

Grand-potential-based phase-field model for multiple phases, grains, and chemical components

Larry K. Aagesen,^{*} Yipeng Gao, and Daniel Schwen*Fuels Modeling and Simulation Department, Idaho National Laboratory, P.O. Box 1625, Idaho Falls, Idaho 83415, USA*

Karim Ahmed

Department of Nuclear Engineering, Texas A&M University, AI Engineering Building, College Station, Texas 77843, USA

(Received 14 February 2018; published 24 August 2018)

Grand-potential-based phase-field model for multiple phases, grains, and chemical components is derived from a grand-potential functional. Due to the grand-potential formulation, the chemical energy does not contribute to the interfacial energy between phases, simplifying parametrization and decoupling interface thickness from interfacial energy, which can potentially allow increased interface thicknesses and therefore improved computational efficiency. Two-phase interfaces are stable with respect to the formation of additional phases, simplifying implementation and allowing the variational form of the evolution equations to be used. Additionally, we show that grand-potential-based phase-field models are capable of simulating phase separation, and we derive conditions under which this is possible.

DOI: [10.1103/PhysRevE.98.023309](https://doi.org/10.1103/PhysRevE.98.023309)

I. INTRODUCTION

The phase-field method is an increasingly popular technique for simulating microstructural evolution in materials. Because engineering materials are often both polycrystalline and multicomponent, phase-field models are required that are capable of tracking an arbitrary number of chemical components, phases, and grains of each phase. Several phase-field models capable of simulating multiphase, multigrain materials have been developed in recent years [1–8], and others have also been developed that add the capability to simulate multiple chemical components [9–25]. Each of these models has various advantages and disadvantages relative to desirable model characteristics.

One highly desirable characteristic of phase-field models of multicomponent systems is the decoupling of interfacial thickness and interfacial energy. In the seminal alloy solidification model of Wheeler, Boettinger, and McFadden (WBM) [26], the interface between phases is considered to be a mixture of the two phases with an equal composition. However, in this formulation, there is a nonzero contribution to the interfacial energy from the chemical energy in the interfacial region. This contribution increases with interface thickness, and thus the interfacial energy is coupled to the interfacial thickness in this formulation. This sets a practical upper limit on the interface thickness for a given materials system and requires a simulation resolution fine enough to resolve that interface. Thus, the coupling between interfacial energy and interfacial thickness in WBM-type models can present limitations in simulating large systems.

To circumvent these limitations, several strategies have been pursued. Tiaden *et al.* [27] first showed that in the WBM model the coupling between solute concentration and order

parameter influences the interface thickness. They developed a multiphase model for binary alloys in which the concentration in the interfacial region is defined as a mixture of each phase's concentration and showed that when the ratio of concentrations between phases is given by a constant partition coefficient, the concentration is decoupled from the evolution equation for the order parameter, removing the limit on interface thickness [27]. Building on this approach, Kim, Kim, and Suzuki (KKS) introduced a phase-field model for two-phase binary alloys in which the interfacial region is defined as a mixture of the two phases with different phase compositions but constrained to have the same chemical potential [28]. In this case, the chemical energy in the interface does not contribute to the interfacial energy, and the interfacial energy and interfacial thickness are decoupled, allowing interface thickness to be increased (subject to adequately resolving curvatures of microstructural features of interest) and simulation resolution made coarser. However, this comes at a cost of introducing the additional phase composition variables, resulting in additional complexities in solving the equations numerically. Kim *et al.* also extended the model to three-phase systems [29]. Folch and Plapp developed a three-phase model that decouples the interfacial thickness from interfacial energy for parabolic phase free energies [30] and introduced interpolation functions that prevented the spurious formation of the third phase at a two-phase interface, as discussed further below. Ohno *et al.* extended the KKS model to three phases [31] using the interpolation functions developed by Folch and Plapp. Moelans developed a multi-order-parameter model that allows an arbitrary number of phases, grains, and chemical components to be represented and uses the KKS approach to exclude the chemical energy contribution to interfacial energy [13]. In this model, the interfacial thickness is decoupled from the interfacial energy in a multiphase, multi-order-parameter model. However, as with the original KKS model, the phase concentration variables for each solute species must be solved

^{*}Larry.Aagesen@inl.gov

for simultaneously with the evolution equations, increasing computational requirements.

Recently, a phase-field model for alloy solidification based on a grand-potential functional was introduced by Plapp [32] that retains the advantage of decoupling the interfacial energy from the interfacial thickness, while removing the need for phase concentration variables for certain chemical free energy forms. In this model, the evolution equations are derived from a functional of the grand-potential density rather than the Helmholtz free energy density more typically used in phase-field models. An evolution equation for the chemical potential difference between species is used, rather than composition. Reference [32] also showed that KKS-type models can be derived starting from the grand-potential functional. The grand-potential approach has been extended to multi-phase-field models [16,18–25]. (We refer to multi-phase-field models as models that enforce the constraint that all phase-field variables ϕ_i sum to 1 at each point, and we refer to multi-order-parameter models as models where this requirement is not enforced.) These models also decouple interfacial thickness from interfacial energy and evolve the chemical potential difference as a function of time and thus do not require solving for phase concentration variables. However, in these models, a two-phase interface is not stable with respect to the formation of additional phases at the interface [7].

The stability of two-phase interfaces with respect to the formation of additional phases is another highly desirable characteristic of phase-field models of multiphase, multigrain systems. The spurious formation of additional phases at two-phase interfaces can potentially lead to nucleation of new phases in unphysical locations and causes the interfacial energy to deviate from its value for the two-phase interface. The spurious formation of additional phases has been a commonly encountered problem in multi-phase-field models that has been addressed in different ways. The models of Steinbach *et al.* [1] and Steinbach and Pezzola [2], and those derived from them, result in two-phase interfaces that are unstable with respect to the formation of additional phases, as discussed by Toth *et al.* [7]. Reference [1] uses the double-well potential, with terms of the form $W_{ij}\phi_i^2\phi_j^2$ (where W_{ij} is a constant), whereas Ref. [2] uses the double-obstacle potential, with terms of the form $W_{ij}\phi_i\phi_j$ and a sharp penalty for phase-field values outside the range $[0,1]$. The use of the double-obstacle potential significantly reduces third-phase formation at interfaces [33]. An alternative approach to preventing spurious third-phase formation in the models of Refs. [1,2] was developed by Kim *et al.* [5,29], who introduced a step function s_{ij} to the Allen-Cahn equation for each order parameter. The step function $s_{ij} = s_i s_j$, where $s_i = 1$ if $\phi_i > 0$ and $s_i = 0$ otherwise. Although this approach retains the variational formulation of the Allen-Cahn equations, it may generate a stationary solution from a nonequilibrium state [7]. It also prevents the propagation of ϕ_i into regions where $\phi_i = 0$ initially unless the step function is modified based on neighboring values of the order parameter on a uniform finite-difference grid [29]. This requirement makes it difficult to generalize the method to adaptive grid spacing, finite element, or finite volume discretization schemes. The multi-phase-field, grand-potential-based models in Refs. [16,18–24] use the multiphase free energy functional including double-obstacle potential of

Ref. [2], whereas Ref. [25] uses the double-well potential of Ref. [1]. In Refs. [16,18–24], the authors mitigated spurious third-phase formation by adding penalty terms of the form $W_{ijk}\phi_i\phi_j\phi_k$, where W_{ijk} is a constant. Such terms can cause the contact angles at triple junctions to deviate from their equilibrium values; a procedure to calibrate W_{ijk} to obtain improved accuracy in triple junction angles is given in Ref. [8]. In Ref. [34] terms of the form $W_{ijk}\phi_i\phi_j\phi_k$ were employed in the model of Ref. [2] to minimize leakage of third phases from triple junctions to adjacent grain boundaries in cases of large differences in interfacial energies between the grain boundaries. A procedure to determine W_{ijk} was given to obtain improved accuracy in triple-junction angles and interfacial velocities in grain growth simulations [34]. The three-phase model of Folch and Plapp [30] prevents spurious third-phase formation through the use of a triple-well potential for the bulk energies and specially chosen fifth-order interpolation functions for the chemical free energies in each phase (with the limitation that the chemical free energies are parabolic with respect to concentration). Along an i - j interface, derivatives of these interpolation functions are zero with respect to ϕ_k . The three-phase extension of the KKS phase-field model developed by Ohno *et al.* [31] uses these same interpolation functions to allow for stable binary interfaces with greater flexibility in choice of chemical energies for each phase. However, the polynomial interpolation functions developed in Ref. [30] cannot be readily generalized to higher numbers of order parameters. The previously discussed multiphase, multi-order-parameter model by Moelans [13] employs bulk and gradient energy terms that are stable with respect to third-phase formation at a two-phase interface. This work also introduced interpolation functions for chemical energies that, in a binary interface, have zero slope with respect to order parameters for additional phases and thus prevent the chemical energy terms from contributing to third-phase formation.

Here we introduce a multiphase, multi-order-parameter model based on a grand-potential functional that features the desirable characteristics discussed above: decoupling of interfacial energy from interfacial thickness and the stability of two-phase interfaces with respect to the formation of additional phases. To our knowledge, the only existing model for multigrain, multiphase, multicomponent systems that features both of these characteristics is the model of Moelans [13], based on the KKS approach. By employing the bulk free energies and interpolation functions from Ref. [13] within a grand-potential functional, we retain the decoupling of interfacial thickness and interfacial energy and the stability of binary interfaces, while removing the need for additional phase concentration variables of the KKS approach. This eliminates the need to solve a nonlinear equation for each of these variables, simplifying implementation and reducing computational complexity.

An additional capability of grand-potential-based phase-field models considered here is the ability to model phase separation. Since their introduction, grand-potential-based phase-field models were considered incapable of simulating phase separation [32]. This conclusion was drawn from the fact that the model formulation prevents the usage of square gradient terms of concentrations in the total grand potential and requires a convex chemical free energy function in each phase. These conditions are necessary such that concentration

and chemical potential are related by a local and invertible relation [32]. However, we demonstrate here analytically and with simulations that the grand-potential formulation can be used to model phase separation.

This work is organized as follows. In Sec. II, we give the formulation of the model and show analytically that it has the desired properties discussed in the introduction. In Sec. III the formulation and implementation of the model is verified by comparing with expected results for the morphology of steady-state microstructures and the kinetics of growth. The capability of both single-order parameter and multi-order-parameter grand-potential models to simulate phase separation is discussed in Sec. IV, and conclusions and future implications of the work are discussed in Sec. V.

II. GRAND POTENTIAL MODEL FORMULATION

The phase-field model is formulated to describe N possible phases and K chemical species. For each phase α , there are p_α possible grain orientations. The individual grains of phase α are represented by a set of nonconserved order parameters $\vec{\eta}_\alpha = (\eta_{\alpha 1}, \eta_{\alpha 2}, \dots, \eta_{\alpha p_\alpha})$, where the first subscript of each order parameter indexes the phase and the second subscript indexes the grains. A similar set of order parameters exists for each of the N possible phases, such that the microstructure is represented by the vector of order parameters $\vec{\eta} = (\vec{\eta}_\alpha, \vec{\eta}_\beta, \dots, \vec{\eta}_N)$. Within the interior of grain i of phase α , $\eta_{\alpha i} = 1$ and all other order parameters have value 0. The interface between grain i of phase α and grain j of phase β is represented by smooth variation of order parameters $\eta_{\alpha i}$ from 1 to 0 and $\eta_{\beta j}$ from 0 to 1.

In addition to the local crystallographic information, the local chemical composition is required to represent the microstructure. As in Ref. [32], we track the number density ρ of each solute species at each position. Assuming each chemical species has the same atomic volume V_a , $K - 1$ variables are then required, and the K th species is considered the solvent. The number density of chemical species A , ρ_A , is related to its local atomic fraction, c_A , as

$$\rho_A = \frac{c_A}{V_a}. \quad (1)$$

The total grand potential Ω of the system is defined as

$$\Omega = \int_V (\omega_{mw} + \omega_{\text{grad}} + \omega_{\text{chem}}) dV. \quad (2)$$

ω_{mw} is a multiwell contribution to the bulk free energy density that has the form

$$\omega_{mw} = m f_0, \quad (3)$$

$$f_0 = \sum_{\alpha=1}^N \sum_{i=1}^{p_\alpha} \left(\frac{\eta_{\alpha i}^4}{4} - \frac{\eta_{\alpha i}^2}{2} \right) + \sum_{\alpha=1}^N \sum_{i=1}^{p_\alpha} \left(\sum_{\beta=1}^N \sum_{j=1, \alpha i \neq \beta j}^{p_\beta} \frac{\gamma_{\alpha i \beta j}}{2} \eta_{\alpha i}^2 \eta_{\beta j}^2 \right) + \frac{1}{4}, \quad (4)$$

where m is a constant with dimensions of energy per unit volume, α and β index phases, i and j index grains, and $\gamma_{\alpha i \beta j}$ are a set of constants that allow the interfacial energy between

grain i of phase α and grain j of phase β to be controlled [13,35]. We require $\gamma_{\alpha i \beta j} = \gamma_{\beta j \alpha i}$ so the terms $\frac{\gamma_{\alpha i \beta j}}{2} \eta_{\alpha i}^2 \eta_{\beta j}^2$ can be combined, resulting in one cross-term $\gamma_{\alpha i \beta j} \eta_{\alpha i}^2 \eta_{\beta j}^2$ for each pair of order parameters. Although interfacial energy anisotropy and/or grain boundary energy anisotropy can be included by making the coefficients $\gamma_{\alpha i \beta j}$ dependent on interface orientation, these effects are not considered here. The gradient energy contribution ω_{grad} is given by

$$\omega_{\text{grad}} = \frac{\kappa}{2} \sum_{\alpha=1}^N \sum_{i=1}^{p_\alpha} |\nabla \eta_{\alpha i}|^2, \quad (5)$$

where κ is the gradient energy coefficient. Consistent with the assumption of isotropic interfacial energy and grain boundary energy, we maintain a constant κ throughout and assume it is independent of composition. The chemical contribution to the grand-potential functional ω_{chem} is given by

$$\omega_{\text{chem}} = \sum_{\alpha=1}^N h_\alpha \omega_\alpha, \quad (6)$$

where h_α is an interpolation function for phase α and ω_α is the grand-potential density for phase α . h_α has the form [13]

$$h_\alpha = \frac{\sum_{i=1}^{p_\alpha} \eta_{\alpha i}^2}{\sum_{\beta} \sum_{i=1}^{p_\beta} \eta_{\beta i}^2}. \quad (7)$$

$h_\alpha = 1$ in the interior of phase α and $h_\alpha = 0$ in the interior of all other phases. h_α can be interpreted as the phase fraction of phase α . The grand-potential density for phase α , ω_α , is

$$\omega_\alpha = f_\alpha - \rho_A \mu_A - \rho_B \mu_B - \dots - \rho_{K-1} \mu_{K-1}, \quad (8)$$

where f_α is the Helmholtz free energy density of phase α , and μ_A is the chemical potential difference between species A and species K . As in Ref. [32], here μ_A has dimensions of energy, rather than energy per unit volume as is often used in phase-field models.

A. Evolution equations

Each order parameter $\eta_{\alpha i}$ evolves by an Allen-Cahn equation derived from the grand-potential functional:

$$\begin{aligned} \frac{\partial \eta_{\alpha i}}{\partial t} &= -L \frac{\delta \Omega}{\delta \eta_{\alpha i}} \\ &= -L \left[m \left(\eta_{\alpha i}^3 - \eta_{\alpha i} + 2\eta_{\alpha i} \sum_{\beta=1}^N \sum_{j=1, \alpha i \neq \beta j}^{p_\beta} \gamma_{\alpha i \beta j} \eta_{\beta j}^2 \right) \right. \\ &\quad \left. - \kappa \nabla^2 \eta_{\alpha i} + \sum_{\beta=1}^N \frac{\partial h_\beta}{\partial \eta_{\alpha i}} \omega_\beta \right], \end{aligned} \quad (9)$$

where the Allen-Cahn mobility is given by [13]

$$L = \frac{\sum_{\alpha i} \sum_{\beta j \neq \alpha i} L_{\alpha i \beta j} \eta_{\alpha i}^2 \eta_{\beta j}^2}{\sum_{\alpha i} \sum_{\beta j \neq \alpha i} \eta_{\alpha i}^2 \eta_{\beta j}^2}. \quad (10)$$

$L_{\alpha i \beta j}$ is the mobility coefficient for the interface between grain i of phase α and grain j of phase β and is discussed further in Sec. IID.

For each solute species, the generalized diffusion equation is

$$\frac{\partial \rho_A}{\partial t} = \nabla \cdot \sum_{I=1}^{K-1} M_{AI} \nabla \mu_I, \quad (11)$$

where M_{AI} is a mobility coefficient with dimensions of $(\text{energy} \times \text{length} \times \text{time})^{-1}$. [This is in contrast to the more typically used evolution equation $\frac{\partial c}{\partial t} = \nabla \cdot (M \nabla \frac{\delta F}{\delta c})$, where the mobility coefficient has units of $\text{length}^5 \times (\text{energy} \times \text{time})^{-1}$]. Since the phase-field model is developed starting from a grand-potential functional, the chemical potential of each species, rather than its number density, is the appropriate field variable to express the functional in terms of [32]. Thus, the time evolution of μ_I rather than ρ_I should be considered, and Eq. (11) is transformed to a set of evolution equations for μ_I as follows. Using the chain rule, $\frac{\partial \rho_A}{\partial t}$ can be expressed as

$$\frac{\partial \rho_A}{\partial t} = \sum_{I=1}^{K-1} \frac{\partial \rho_A}{\partial \mu_I} \frac{\partial \mu_I}{\partial t} + \sum_{\beta=1}^N \sum_{i=1}^{p_\beta} \frac{\partial \rho_A}{\partial \eta_{\beta i}} \frac{\partial \eta_{\beta i}}{\partial t}. \quad (12)$$

Substituting Eq. (11) in Eq. (12) and rearranging,

$$\sum_{I=1}^{K-1} \frac{\partial \rho_A}{\partial \mu_I} \frac{\partial \mu_I}{\partial t} = \nabla \cdot \sum_{I=1}^{K-1} M_{AI} \nabla \mu_I - \sum_{\beta=1}^N \sum_{i=1}^{p_\beta} \frac{\partial \rho_A}{\partial \eta_{\beta i}} \frac{\partial \eta_{\beta i}}{\partial t}. \quad (13)$$

The susceptibility χ_{AI} is defined as

$$\chi_{AI} \equiv \frac{\partial \rho_A}{\partial \mu_I}. \quad (14)$$

Using Eq. (14) in (13),

$$\sum_{I=1}^{K-1} \chi_{AI} \frac{\partial \mu_I}{\partial t} = \nabla \cdot \sum_{I=1}^{K-1} M_{AI} \nabla \mu_I - \sum_{\beta=1}^N \sum_{i=1}^{p_\beta} \frac{\partial \rho_A}{\partial \eta_{\beta i}} \frac{\partial \eta_{\beta i}}{\partial t}. \quad (15)$$

The susceptibility χ_{AI} needs to be expressed in terms of order parameters and chemical potential. To do so, the density ρ_A can be determined from Ω using the thermodynamic relation

$$\rho_A = -\frac{\delta \Omega}{\delta \mu_A} = -\sum_{\beta=1}^N h_\beta \frac{\partial \omega_\beta}{\partial \mu_A} = \sum_{\beta=1}^N h_\beta \rho_A^\beta, \quad (16)$$

where $\rho_A^\beta = -\frac{\partial \omega_\beta}{\partial \mu_A}$ is the number density of A atoms in the interior of phase β . Substituting (16) into (14),

$$\chi_{AI} = \frac{\partial}{\partial \mu_I} \sum_{\beta=1}^N h_\beta \rho_A^\beta = \sum_{\beta=1}^N h_\beta \chi_{AI}^\beta, \quad (17)$$

where $\chi_{AI}^\beta = \frac{\partial \rho_A^\beta}{\partial \mu_I}$. The specific form of χ_{AI}^β depends on f_β , as further discussed in Sec. II A 1.

The mobility coefficients M_{AI} are given by

$$M_{AI} = \sum_{\beta=1}^N h_\beta M_{AI}^\beta. \quad (18)$$

The mobilities in phase β , M_{AI}^β , can be determined as a function of the self-diffusivity D_{AA}^β and interdiffusivities D_{AI}^β ,

$A \neq I$ [36]:

$$D_{AI}^\beta = \sum_{J=1}^{K-1} M_{AJ}^\beta \frac{\partial \mu_J}{\partial \rho_I^\beta} = \sum_{J=1}^{K-1} M_{AJ}^\beta \frac{1}{\chi_{IJ}^\beta}. \quad (19)$$

This results in a set of equations that can be solved for M_{AJ}^β . For the case where interdiffusivities are negligible, $M_{AI}^\beta = 0$ for $I \neq A$, and $M_{AA}^\beta = D_{AA}^\beta \chi_{AA}^\beta$.

I. Evolution equations for common free energy forms

The dependence of grand potential, density, composition, and susceptibility on chemical potential is given here for common Helmholtz free energy functional forms. The functions presented here are multispecies generalizations of the results of Ref. [32].

For a parabolic free energy with $f_\alpha = f_{\min}^\alpha + \sum_{I=1}^{K-1} \frac{1}{2} k_I^\alpha (c_I - c_I^{\alpha, \min})^2$, where I indexes chemical species, k_I^α is the curvature of the parabola with units of energy density, $c_I^{\alpha, \min}$ is the composition at which the minimum occurs, f_{\min}^α is a constant with units of energy density, and using $\mu_I = \frac{\delta f_\alpha}{\delta \rho_I} = V_a \frac{\delta f_\alpha}{\delta c_I}$,

$$\omega_\alpha = f_{\min}^\alpha + \sum_{I=1}^{K-1} -\frac{1}{2} \frac{\mu_I^2}{V_a^2 k_I^\alpha} - \frac{\mu_I}{V_a} c_I^{\alpha, \min}, \quad (20)$$

$$\rho_A^\alpha = -\frac{\partial \omega_\alpha}{\partial \mu_A} = \frac{\mu_A}{V_a^2 k_A^\alpha} + \frac{c_A^{\alpha, \min}}{V_a}, \quad (21)$$

$$c_A = V_a \rho_A = \sum_{\beta=1}^N h_\beta \left(\frac{\mu_A}{V_a k_A^\beta} + c_A^{\beta, \min} \right), \quad (22)$$

$$\chi_{AI}^\alpha = \frac{\partial \rho_A^\alpha}{\partial \mu_I} = \begin{cases} \frac{1}{V_a^2 k_A^\alpha}, & I = A \\ 0, & I \neq A \end{cases}. \quad (23)$$

For a dilute solution with $f_\alpha = f_{\min}^\alpha + \sum_{I=1}^{K-1} \frac{E_I^\alpha c_I}{V_a} + \frac{kT}{V_a} (c_I \ln c_I - c_I)$, where E_I^α is a constant with units of energy,

$$\omega_\alpha = f_{\min}^\alpha + \sum_{I=1}^{K-1} -\frac{kT}{V_a} \exp\left(\frac{\mu_I - E_I^\alpha}{kT}\right), \quad (24)$$

$$\rho_A^\alpha = -\frac{\partial \omega_\alpha}{\partial \mu_A} = \frac{1}{V_a} \exp\left(\frac{\mu_A - E_A^\alpha}{kT}\right), \quad (25)$$

$$c_A = V_a \rho_A = \sum_{\beta=1}^N h_\beta \exp\left(\frac{\mu_A - E_A^\beta}{kT}\right), \quad (26)$$

$$\chi_{AI}^\alpha = \frac{\partial \rho_A^\alpha}{\partial \mu_I} = \begin{cases} \frac{1}{kT V_a} \exp\left(\frac{\mu_A - E_A^\alpha}{kT}\right), & I = A \\ 0, & I \neq A \end{cases}. \quad (27)$$

For either the parabolic or dilute solution Helmholtz free energy, since $\chi_{AI}^\alpha = 0$ for $A \neq I$, the evolution equation for chemical potential, Eq. (15), can be simplified to

$$\chi_{AA}^\alpha \frac{\partial \mu_A}{\partial t} = \nabla \cdot \sum_{I=1}^{K-1} M_{AI} \nabla \mu_I - \sum_{\beta=1}^N \sum_{i=1}^{p_\beta} \frac{\partial \rho_A}{\partial \eta_{\beta i}} \frac{\partial \eta_{\beta i}}{\partial t}. \quad (28)$$

In the case when all interdiffusivities are zero, only M_{AA} is nonzero, and Eq. (28) further simplifies to

$$\chi_{AA} \frac{\partial \mu_A}{\partial t} = \nabla \cdot (M_{AA} \nabla \mu_A) - \sum_{\beta=1}^N \sum_{i=1}^{p_\beta} \frac{\partial \rho_A}{\partial \eta_{\beta i}} \frac{\partial \eta_{\beta i}}{\partial t}. \quad (29)$$

B. Steady-state conditions and interfacial profiles

The conditions for steady state can be found from Eq. (15) and (9). Consider a planar interface with its normal in the x direction between grain 1 of phase α and grain 1 of phase β , represented by order parameters $\eta_{\alpha 1}$ and $\eta_{\beta 1}$, respectively. The center of the interface is at $x = 0$, with phase α where $x < 0$ and phase β where $x > 0$. For the system to be in chemical equilibrium, the chemical potential μ_I for each solute species must be constant, and the grand-potential densities in each phase must be equal: $\omega_\alpha = \omega_\beta$ [37]. For a two-species system, the conditions of equal chemical potential and equal grand-potential density are equivalent to the common tangent construction. For the system to be in steady state, $\frac{\partial \mu_I}{\partial t} = 0 \forall I$, which is met when μ_I is constant, and $\frac{\partial \eta_{\alpha 1}}{\partial t} = \frac{\partial \eta_{\beta 1}}{\partial t} = 0$ by Eq. (15). By Eq. (9), when $\frac{\partial \eta_{\alpha 1}}{\partial t} = 0$,

$$m(\eta_{\alpha 1}^3 - \eta_{\alpha 1} + 2\eta_{\alpha 1}\gamma_{\alpha 1\beta 1}\eta_{\beta 1}^2) - \kappa \nabla^2 \eta_{\alpha 1} + \frac{\partial h_\alpha}{\partial \eta_{\alpha 1}} \omega_\alpha + \frac{\partial h_\beta}{\partial \eta_{\alpha 1}} \omega_\beta = 0. \quad (30)$$

Because $\frac{\partial h_\alpha}{\partial \eta_{\alpha 1}} = -\frac{\partial h_\beta}{\partial \eta_{\alpha 1}} = \frac{2\eta_{\alpha 1}\eta_{\beta 1}^2}{\eta_{\alpha 1}^2 + \eta_{\beta 1}^2}$,

$$m(\eta_{\alpha 1}^3 - \eta_{\alpha 1} + 2\eta_{\alpha 1}\gamma_{\alpha 1\beta 1}\eta_{\beta 1}^2) - \kappa \nabla^2 \eta_{\alpha 1} + \frac{\partial h_\alpha}{\partial \eta_{\alpha 1}} (\omega_\alpha - \omega_\beta) = 0. \quad (31)$$

A similar expression can be derived from the condition $\frac{\partial \eta_{\beta 1}}{\partial t} = 0$:

$$m(\eta_{\beta 1}^3 - \eta_{\beta 1} + 2\eta_{\beta 1}\gamma_{\alpha 1\beta 1}\eta_{\alpha 1}^2) - \kappa \nabla^2 \eta_{\beta 1} + \frac{\partial h_\alpha}{\partial \eta_{\beta 1}} (-\omega_\alpha + \omega_\beta) = 0. \quad (32)$$

Since $\omega_\alpha = \omega_\beta$ throughout in chemical equilibrium, Eqs. (31) and (32) become

$$m(\eta_{\alpha 1}^3 - \eta_{\alpha 1} + 2\eta_{\alpha 1}\gamma_{\alpha 1\beta 1}\eta_{\beta 1}^2) - \kappa \nabla^2 \eta_{\alpha 1} = 0, \quad (33)$$

$$m(\eta_{\beta 1}^3 - \eta_{\beta 1} + 2\eta_{\beta 1}\gamma_{\alpha 1\beta 1}\eta_{\alpha 1}^2) - \kappa \nabla^2 \eta_{\beta 1} = 0. \quad (34)$$

Thus, for steady-state conditions, $\mu_I = 0$, $\omega_\alpha = \omega_\beta$, and the steady-state equilibrium interfacial profiles for $\eta_{\alpha 1}$ and $\eta_{\beta 1}$ can be determined from the analysis of Ref. [35]. For the case $\gamma_{\alpha 1\beta 1} = 1.5$, an analytical solution can be found for both order parameters:

$$\eta_{\alpha 1} = \frac{1}{2} \left[1 - \tanh \left(\sqrt{\frac{m}{2\kappa}} x \right) \right], \quad (35)$$

$$\eta_{\beta 1} = \frac{1}{2} \left[1 + \tanh \left(\sqrt{\frac{m}{2\kappa}} x \right) \right]. \quad (36)$$

These are referred to as the symmetric profiles in Ref. [35], where a symmetric profile has the property $\eta_{\alpha 1}(x) = 1 -$

$\eta_{\alpha 1}(-x)$ with the midpoint of the interface defined at $x = 0$. $\eta_{\alpha 1} + \eta_{\beta 1} = 1$ also holds throughout, and at $x = 0$, $\eta_{\alpha 1} = \eta_{\beta 1} = 0.5$.

For $\gamma_{\alpha 1\beta 1} \neq 1.5$, an analytical solution to the interfacial profiles does not exist. The interfaces are not symmetric, and $\eta_{\alpha 1} + \eta_{\beta 1} \neq 1$ through the interface. For $\gamma_{\alpha 1\beta 1} < 1.5$, the interface width becomes smaller, and at $x = 0$, $\eta_{\alpha 1} = \eta_{\beta 1} > 0.5$; conversely, for $\gamma_{\alpha 1\beta 1} > 1.5$, the interface width becomes larger, and at $x = 0$, $\eta_{\alpha 1} = \eta_{\beta 1} < 0.5$. Further details are available in Ref. [35].

C. Stability of two-phase interface with respect to third-phase formation

One advantage of this formulation is that a two-phase interface is stable with respect to formation of a third phase. To show this, we first demonstrate the stability of the multiwell and gradient terms in the total grand-potential functional, then show that the chemical energy contribution does not alter stability. Consider a three-phase system with phases α , β , and δ . $\eta_{\delta 1}$ is an order parameter representing grain 1 of phase δ . Throughout a planar α - β interface as described in Sec. II B, the δ phase is not present initially, and $\eta_{\delta 1} = 0$. The grand potential of the system with only the multiwell and gradient terms, Ω_{mg} , is

$$\Omega_{mg} = \int_V (\omega_{mw} + \omega_{grad}) dV. \quad (37)$$

For the three-phase system in the absence of chemical energy, the variational derivatives are

$$\frac{\delta \Omega_{mg}}{\delta \eta_{\alpha 1}} = m[\eta_{\alpha 1}^3 - \eta_{\alpha 1} + 2\eta_{\alpha 1}(\gamma_{\alpha 1\beta 1}\eta_{\beta 1}^2 + \gamma_{\alpha 1\delta 1}\eta_{\delta 1}^2)] - \kappa \nabla^2 \eta_{\alpha 1}, \quad (38)$$

$$\frac{\delta \Omega_{mg}}{\delta \eta_{\beta 1}} = m[\eta_{\beta 1}^3 - \eta_{\beta 1} + 2\eta_{\beta 1}(\gamma_{\alpha 1\beta 1}\eta_{\alpha 1}^2 + \gamma_{\beta 1\delta 1}\eta_{\delta 1}^2)] - \kappa \nabla^2 \eta_{\beta 1}, \quad (39)$$

$$\frac{\delta \Omega_{mg}}{\delta \eta_{\delta 1}} = m[\eta_{\delta 1}^3 - \eta_{\delta 1} + 2\eta_{\delta 1}(\gamma_{\alpha 1\delta 1}\eta_{\alpha 1}^2 + \gamma_{\beta 1\delta 1}\eta_{\beta 1}^2)] - \kappa \nabla^2 \eta_{\delta 1}. \quad (40)$$

The order parameters $\eta_{\alpha 1}$, $\eta_{\beta 1}$, $\eta_{\delta 1}$ will be in steady state if $\frac{\delta \Omega_{mg}}{\delta \eta_{\alpha 1}} = \frac{\delta \Omega_{mg}}{\delta \eta_{\beta 1}} = \frac{\delta \Omega_{mg}}{\delta \eta_{\delta 1}} = 0$ holds throughout. From Eq. (40), since $\eta_{\delta 1} = 0$, $\frac{\delta \Omega_{mg}}{\delta \eta_{\delta 1}} = 0$. Also using $\eta_{\delta 1} = 0$, Eq. (38) and (39) reduce to Eq. (33) and (34). Thus, steady state α - β interfaces in the two-phase system are also steady-state solutions $\frac{\delta \Omega_{mg}}{\delta \eta_{\alpha 1}} = \frac{\delta \Omega_{mg}}{\delta \eta_{\beta 1}} = 0$ for the three-phase system when $\eta_{\delta 1} = 0$.

Having established the stability of two-phase interfaces considering only the multiwell and gradient terms, we now consider the effect of the chemical energy contribution. For the three-phase system, the variational derivatives of the original

grand potential Ω are

$$\frac{\delta\Omega}{\delta\eta_{\alpha 1}} = \frac{\delta\Omega_{mg}}{\delta\eta_{\alpha 1}} + \frac{\partial h_{\alpha}}{\partial\eta_{\alpha 1}}\omega_{\alpha} + \frac{\partial h_{\beta}}{\partial\eta_{\alpha 1}}\omega_{\beta} + \frac{\partial h_{\delta}}{\partial\eta_{\alpha 1}}\omega_{\delta}, \quad (41)$$

$$\frac{\delta\Omega}{\delta\eta_{\beta 1}} = \frac{\delta\Omega_{mg}}{\delta\eta_{\beta 1}} + \frac{\partial h_{\alpha}}{\partial\eta_{\beta 1}}\omega_{\alpha} + \frac{\partial h_{\beta}}{\partial\eta_{\beta 1}}\omega_{\beta} + \frac{\partial h_{\delta}}{\partial\eta_{\beta 1}}\omega_{\delta}, \quad (42)$$

$$\frac{\delta\Omega}{\delta\eta_{\delta 1}} = \frac{\delta\Omega_{mg}}{\delta\eta_{\delta 1}} + \frac{\partial h_{\alpha}}{\partial\eta_{\delta 1}}\omega_{\alpha} + \frac{\partial h_{\beta}}{\partial\eta_{\delta 1}}\omega_{\beta} + \frac{\partial h_{\delta}}{\partial\eta_{\delta 1}}\omega_{\delta}. \quad (43)$$

In Eq. (43), $\eta_{\delta 1} = 0$ and $\frac{\partial h_{\alpha}(\eta_{\delta 1}=0)}{\partial\eta_{\delta 1}} = \frac{\partial h_{\beta}(\eta_{\delta 1}=0)}{\partial\eta_{\delta 1}} = \frac{\partial h_{\delta}(\eta_{\delta 1}=0)}{\partial\eta_{\delta 1}} = 0$, so $\frac{\delta\Omega}{\delta\eta_{\delta 1}} = 0$. Because $\frac{\partial h_{\delta}(\eta_{\alpha 1}=0)}{\partial\eta_{\alpha 1}} = 0$, Eq. (41) reduces to Eq. (31). Similarly, Eq. (42) reduces to Eq. (32). Thus, when $\eta_{\delta 1} = 0$, order parameter profiles that satisfy (31) and (32) result in $\frac{\delta\Omega}{\delta\eta_{\alpha 1}} = \frac{\delta\Omega}{\delta\eta_{\beta 1}} = 0$ for the three-phase system, and $\frac{\delta\Omega}{\delta\eta_{\delta 1}} = 0$ also holds. Thus, the planar α - β interface remains an equilibrium solution for the three-phase system when the chemical energy contribution is also considered and is stable with respect to spurious formation of additional phases.

To guarantee that these are stable rather than metastable solutions, the additional conditions $\frac{\delta^2\Omega}{\delta\eta_{\delta 1}^2} > 0$ and $\frac{\delta^2\Omega}{\delta c^2} > 0$ must be satisfied to ensure that small perturbations of $\eta_{\delta 0}$ about 0 and small composition fluctuations decay away [30]. As discussed by Folch and Plapp, it is not possible to show this is true for arbitrary chemical free energy parameters [30]. However, as discussed further in Sec. III B, testing of α - β interfaces with $\eta_{\delta 1} \neq 0$ in the initial conditions showed that the equilibrium α - β interface with $\eta_{\delta 1} = 0$ was recovered for the material parameters used for verification.

D. Interfacial parameters

To perform quantitative phase-field simulations, the model parameters need to be related to physical parameters of the system. To determine the interfacial energy in terms of model parameters, consider the interface between grain 1 of phase α and grain 1 of phase β described in Sec. II B, with the interface normal to the x direction. For a multicomponent alloy, the interfacial energy per unit area between phase α and phase β is defined thermodynamically as the excess of the grand potential per unit area [37]. The interfacial energy $\sigma_{\alpha 1\beta 1}$ is given by

$$\sigma_{\alpha 1\beta 1} = \frac{1}{A} \int_V (\omega_{mw} + \omega_{\text{grad}} + \omega_{\text{chem}} - \omega_{\text{eq}}) dV, \quad (44)$$

where ω_{eq} is the equilibrium grand potential and A is the area of the interface between phase α and phase β . Consider a rectangular cuboidal integration volume V , with faces normal to the x , y , and z directions, within the bounds $-L_x/2 \leq x \leq L_x/2$, $-L_y/2 \leq y \leq L_y/2$, $-L_z/2 \leq z \leq L_z/2$, where L_x , L_y , and L_z are the dimensions of the rectangular cuboid in the x , y , and z directions. The area of the interface $A = L_y L_z$, and we allow $L_x \rightarrow \infty$ to ensure the entire interfacial region is contained in the integration volume. Because the interfacial normal is in the x direction, the system is uniform in the y and z directions, so

$$\begin{aligned} \sigma_{\alpha 1\beta 1} &= \frac{1}{L_y L_z} \int_{-\infty}^{\infty} (\omega_{mw} + \omega_{\text{grad}} + \omega_{\text{chem}} - \omega_{\text{eq}}) L_y L_z dx \\ &= \int_{-\infty}^{\infty} (\omega_{mw} + \omega_{\text{grad}} + h_{\alpha}\omega_{\alpha} + h_{\beta}\omega_{\beta} - \omega_{\text{eq}}) dx. \end{aligned} \quad (45)$$

In equilibrium, $\omega_{\alpha} = \omega_{\beta} = \omega_{\text{eq}}$. Since by definition $h_{\alpha} + h_{\beta} = 1$,

$$\sigma_{\alpha 1\beta 1} = \int_{-\infty}^{\infty} (\omega_{mw} + \omega_{\text{grad}}) dx. \quad (46)$$

As expected, there is no contribution from the bulk chemical energies to the interfacial energy of the system. The interfacial energies described by Eq. (46) are thus equivalent to the those described in Ref. [35], and the analysis developed there can be applied to this model. For convenience, we restate those results here. The interfacial energy can be written as [35]

$$\sigma_{\alpha 1\beta 1} = g(\gamma_{\alpha 1\beta 1}) \sqrt{m\kappa}, \quad (47)$$

where $g(\gamma_{\alpha i\beta j})$ is a dimensionless function of $\gamma_{\alpha i\beta j}$. For the symmetric interface, $g(1.5) = \sqrt{2}/3$ [35]. The values of $g(\gamma_{\alpha i\beta j})$ have been tabulated based on numerical simulations [35,38]. Near $\gamma_{\alpha i\beta j} = 1.5$, $g(\gamma_{\alpha i\beta j})$ can be approximated as

$$g(\gamma_{\alpha 1\beta 1}) \approx \frac{4}{3} \sqrt{f_{0,\text{saddle}}} = \frac{4}{3} \sqrt{\frac{2\gamma_{\alpha 1\beta 1} - 1}{4(2\gamma_{\alpha 1\beta 1} + 1)}}, \quad (48)$$

where $f_{0,\text{saddle}}$ is the value of f_0 at the saddle point of the free energy landscape. In some cases, a desired $g(\gamma_{\alpha i\beta j}) = \frac{\sigma_{\alpha i\beta j}}{\sqrt{m\kappa}}$ is known for given $\sigma_{\alpha i\beta j}$, m , and κ , and it is necessary to determine the value of $\gamma_{\alpha i\beta j}$ that will result in the desired $g(\gamma_{\alpha i\beta j})$. This can be done based on the results of Refs. [35,38] using the polynomial interpolation

$$\begin{aligned} \gamma_{\alpha i\beta j} &= (-5.288g^8 - 0.09364g^6 + 9.965g^4 \\ &\quad - 8.183g^2 + 2.007)^{-1}. \end{aligned} \quad (49)$$

The characteristic width of the interface $\ell_{\alpha 1\beta 1}$ is defined based on the absolute value of the gradients of the order parameters at the interface and is given by [35]

$$\ell_{\alpha 1\beta 1} = \sqrt{\frac{\kappa}{mf_{0,\text{inter } f}}}, \quad (50)$$

where $f_{0,\text{inter } f}$ is the value of f_0 at the interface. For a symmetric interface $f_{0,\text{inter } f} = \frac{1}{8}$; for $\gamma_{\alpha 1\beta 1} \neq 1.5$, tabulated values of $f_{0,\text{inter } f}$ are available [35,38].

Equations (47) and (50) can be rearranged to obtain

$$\kappa = \frac{\sigma_{\alpha 1\beta 1} \ell_{\alpha 1\beta 1} \sqrt{f_{0,\text{inter } f}}}{g(\gamma_{\alpha 1\beta 1})}, \quad (51)$$

$$m = \frac{\sigma_{\alpha 1\beta 1}}{\ell_{\alpha 1\beta 1} g(\gamma_{\alpha 1\beta 1}) \sqrt{f_{0,\text{inter } f}}}. \quad (52)$$

A convenient method to parametrize a system with multiple types of interfaces is to choose one interface to be a symmetric interface, for example, the $\eta_{\alpha 1}$ - $\eta_{\beta 1}$ interface. This amounts to setting $\gamma_{\alpha 1\beta 1} = 1.5$. κ and m are calculated using Eqs. (51) and (52) based on the physical value of the interfacial energy $\sigma_{\alpha 1\beta 1}$ and the chosen interfacial thickness $\ell_{\alpha 1\beta 1}$ (subject to the need to be significantly smaller than the curvatures of microstructural features of the system being simulated). For

$\gamma_{\alpha\beta 1} = 1.5$, Eqs. (51) and (52) reduce to [35]

$$\kappa = \frac{3}{4} \sigma_{\alpha\beta 1} \ell_{\alpha\beta 1}, \quad (53)$$

$$m = \frac{6\sigma_{\alpha\beta 1}}{\ell_{\alpha\beta 1}}. \quad (54)$$

In this case, the values of κ and m are determined by the parameters of the symmetric interface. The interfacial energies and grain boundary energies for all other types of interfaces can then be set by calculating $g = \frac{\sigma}{\sqrt{m\kappa}}$ for each interface and determining the value of the γ parameter needed to obtain that value of g using Eq. (49). It should be noted that the interfacial width will also change with $\gamma_{\alpha\beta j}$, and the simulation mesh resolution must be set to adequately resolve the thinnest interface.

The Allen-Cahn mobilities for interfaces between grains can be parameterized using [13]

$$m_{\alpha 1 \alpha 2} \sigma_{\alpha 1 \alpha 2} = \kappa L_{\alpha 1 \alpha 2}, \quad (55)$$

where $m_{\alpha 1 \alpha 2}$ is the grain boundary mobility, with dimensions $\text{length}^4 \times (\text{energy} \times \text{time})^{-1}$.

To determine the Allen-Cahn mobility for interfaces between phases, note from Eq. (9) that the driving force for phase transformation between phase α and β is the difference between grand potentials of those phases. Thus, the thin-interface analysis of Ref. [13] also applies to this model. That analysis allows the Allen-Cahn mobility at the interface between phases $L_{\alpha\beta 1}$ to be related to the interfacial mobility $m_{\alpha\beta 1}$ from the sharp-interface equation $\Delta f_i^{\alpha \rightarrow \beta} = \sigma_{\alpha\beta 1} (1/R_1 + 1/R_2) + v_n/m_{\alpha\beta 1}$ [39], where $\Delta f_i^{\alpha \rightarrow \beta}$ is the driving force for phase transformation, R_1 and R_2 are the principal radii of curvature of the interface, and v_n is the magnitude of the velocity normal to the interface. Using that analysis,

$$\frac{1}{m_{\alpha\beta 1}} = \frac{\sqrt{m}g(\gamma_{\alpha\beta 1})}{\sqrt{\kappa}L_{\alpha\beta 1}} - \sqrt{\frac{\kappa}{2m}} I_\phi(\gamma_{\alpha\beta 1})\zeta. \quad (56)$$

$I_\phi(\gamma_{\alpha\beta 1})$ is a numerical function whose values have been tabulated for a range of $\gamma_{\alpha\beta 1}$ [38]. ζ represents the effect of the difference in compositions between phases on the interfacial velocity in the phase-field model and is given by $\zeta = \frac{1}{V_a^2} \sum_{I=1}^{K-1} (c_I^{\alpha, \text{eq}} - c_I^{\beta, \text{eq}}) \sum_{J=1}^{K-1} m_{IJ} (c_J^{\alpha, \text{eq}} - c_J^{\beta, \text{eq}})$ [13,40], where $c_I^{\alpha, \text{eq}}$ and $c_I^{\beta, \text{eq}}$ are the equilibrium compositions of solute I in phase α and β , respectively, and m_{IJ} are the elements of the inverse of the diffusion mobility matrix M_{IJ} . The thin-interface analysis was performed under the assumption that the diffusion mobilities are the same between phases, $M_{IJ}^\alpha = M_{IJ}^\beta = M_{IJ}$; however, it was found that when diffusion mobilities were of the same order of magnitude, the use of an averaged diffusion mobility $M_{IJ} = 0.5(M_{IJ}^\alpha + M_{IJ}^\beta)$ resulted in only small deviations from the expected kinetic behavior [13]. For a binary alloy with solute species A , $m_{AA} = 1/M_{AA}$ and $\zeta = \frac{(c_A^{\alpha, \text{eq}} - c_A^{\beta, \text{eq}})^2}{V_a^2 M_{AA}}$. In the case of K solute species, if the off-diagonal terms of the mobility matrix vanish ($M_{IJ} = 0$ for $I \neq J$), $\zeta = \sum_{I=1}^{K-1} \frac{(c_I^{\alpha, \text{eq}} - c_I^{\beta, \text{eq}})^2}{V_a^2 M_{II}}$ [40].

TABLE I. Parameters for α , β , and δ phases used for model verification.

| Parameter | Value |
|--|-----------|
| $c_A^{\alpha, \text{min}}$ | 0.1 |
| k_A^α | 10 |
| $c_A^{\beta, \text{min}}$ | 0.9 |
| k_A^β | 10 |
| $c_A^{\delta, \text{min}}$ | 0.5 |
| k_A^δ | 10 |
| V_a | 1 |
| $D_A^\alpha, D_A^\beta, D_A^\delta$ | 1 |
| $L_{\alpha\beta j}$ | 0.21 or 1 |
| $L_{\beta i \beta j}, L_{\alpha i \delta j}, L_{\beta i \delta j}$ | 1 |

For diffusion-limited growth, $1/m_{\alpha\beta 1} = 0$ and [13]

$$L_{\alpha\beta 1} = L_{\alpha\beta 1}^{\text{eq}} = \frac{\sqrt{2}mg(\gamma_{\alpha\beta 1})}{\kappa I_\phi(\gamma_{\alpha\beta 1})\zeta}, \quad (57)$$

where $L_{\alpha\beta 1}^{\text{eq}}$ is the mobility coefficient that ensures that local equilibrium is maintained at the interface.

III. MODEL VERIFICATION

To verify the model, a binary alloy of A and B atoms is considered, with the density of A atoms represented by ρ_A and the atomic fraction of A represented by $c_A = V_a \rho_A$. Three possible phases are considered: α , β , and δ . The α phase has a parabolic free energy $f_\alpha = \frac{1}{2} k_A^\alpha (c_A - c_A^{\alpha, \text{min}})^2$, where $c_A^{\alpha, \text{min}} = 0.1$ and $k_A^\alpha = 10$. The β phase has a parabolic free energy, $f_\beta = \frac{1}{2} k_A^\beta (c_A - c_A^{\beta, \text{min}})^2$, where $c_A^{\beta, \text{min}} = 0.9$ and $k_A^\beta = 10$. Finally, the δ phase also has a parabolic free energy, $f_\delta = \frac{1}{2} k_A^\delta (c_A - c_A^{\delta, \text{min}})^2$, where $c_A^{\delta, \text{min}} = 0.5$ and $k_A^\delta = 10$. Other chosen material parameters are listed in Table I. Different values of κ , m , $\gamma_{\alpha\beta j}$, $\gamma_{\alpha i \delta j}$, and $\gamma_{\beta i \delta j}$ are considered, as described in Secs. III A–III C.

The governing equations were solved numerically using the MOOSE framework [41]. Each system is discretized spatially using uniform linear Lagrange finite elements, with different element sizes as discussed further in Secs. III A–III C. Time discretization used the second-order accurate backward difference formula, with adaptive time stepping using the IterationAdaptiveDT algorithm implemented in the MOOSE framework [42]. The discretized system of equations was solved for each time step using the preconditioned Jacobian-free Newton-Krylov method. The MOOSE framework repository is publicly available at Ref. [43]; an example of the implementation of the model can be found within the repository at Ref. [44]; further information on installation and usage of the MOOSE framework is available at Ref. [45].

A. Morphology

To verify the equilibrium behavior of the model, we consider the morphology of an α -phase grain between two β phase grains, $\beta 1$ and $\beta 2$. In this case the α -phase grain assumes a lenticular shape, as shown in Fig. 1. Experimentally, this

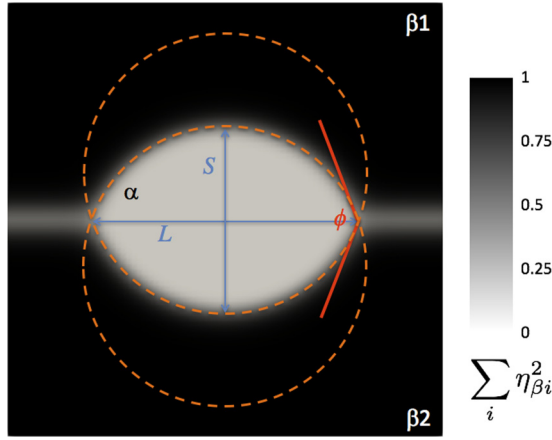


FIG. 1. Geometrical analysis of a grain boundary allotriomorph, with length L , thickness S , and dihedral angle ϕ indicated. $\gamma_{\alpha\beta} = 4.5$, $\gamma_{\beta\beta} = 1.5$, $\phi^{\text{an}} = 135^\circ$. The color bar represents the value of $\sum_i \eta_{\beta i}^2$ and is used to provide a visualization of the microstructure.

morphology is observed when a daughter phase precipitates at a high-angle grain boundary between two grains of a supersaturated parent phase and is sometimes referred to as a grain boundary allotriomorph [46–50]. This morphology is also observed in nuclear fuels such as UO_2 when insoluble gaseous fission products such as Xe and Kr form gas bubbles at grain boundaries [51–55].

In our simulations, a circle-shaped α -phase particle with radius $r = 10$ is placed on the grain boundary between two β phase grains as the initial configuration. The domain size is 40×40 , and the mesh is composed of uniform elements with size $\Delta x = \Delta y = 0.5$. Changing the element size from $\Delta x = \Delta y = 0.5$ to $\Delta x = \Delta y = 0.125$ caused the measured dihedral angle, as described later in the present section, to change by only 0.12% for the case $\kappa = 1$, $m = 1$, $\gamma_{\alpha\beta} = 1.5$, $\gamma_{\beta 1\beta 2} = 1.5$; therefore for computational efficiency $\Delta x = \Delta y = 0.5$ was used in the remainder of this section. No-flux boundary conditions are used. Because this configuration is not at thermodynamic equilibrium, microstructure evolution is expected during relaxation. After full relaxation, the α -phase particle attains a lenticular shape, and its morphology is determined by the interplay of interfacial energy and grain boundary energy. We assume the interfacial energies $\sigma_{\alpha 1\beta 1} = \sigma_{\alpha 1\beta 2} = \sigma_{\alpha\beta}$. As shown in Fig. 1, the length, thickness, and dihedral angle are noted as L , S , and ϕ , respectively. To verify that the model produces the correct morphology for a grain boundary allotriomorph, we calculate ϕ^{sim} from L and S measured from simulations and compare ϕ^{sim} to the dihedral angle predicted by the balance of interfacial energy and grain boundary energy, ϕ^{an} :

$$\cos\left(\frac{\phi^{\text{an}}}{2}\right) = \frac{\sigma_{\beta 1\beta 2}}{2\sigma_{\alpha\beta}}. \quad (58)$$

In the simulation of Fig. 1, the parameters are chosen as $\gamma_{\alpha 1\beta 1} = \gamma_{\alpha 1\beta 2} = \gamma_{\alpha\beta} = 4.5$, $\gamma_{\beta 1\beta 2} = 1.5$, $\kappa = 1.0$, and $m = 1.0$. The interfacial energy and grain boundary energy can be estimated using Eq. (47) and Ref. [38], and the dihedral angle is determined to be $\phi^{\text{an}} = 135^\circ$.

To determine ϕ^{sim} from L and S , the results of previous geometric analyses are used [46,49]. The shape of an idealized grain boundary allotriomorph is assumed to be that of two spherical caps, with both spheres having the same radius. In two dimensions, a grain boundary allotriomorph can be considered as the intersection region between two circles (orange dashed circles in Fig. 1). Assume the radius of each circle is r , and the distance between the two circle centers is d . The length and thickness of the grain boundary allotriomorph can be expressed as functions of r and d ,

$$L = \sqrt{4r^2 - d^2}, \quad (59)$$

$$S = 2r - d, \quad (60)$$

and r and d can be solved through Eqs. (59) and (60) as

$$r = \frac{L^2 + S^2}{4S}, \quad (61)$$

$$d = \frac{L^2 - S^2}{2S}. \quad (62)$$

On the other hand, the dihedral angle is also related to r and d through

$$\cos\frac{\phi}{2} = \frac{d}{2r}. \quad (63)$$

The dihedral angle ϕ can be expressed in terms of L and S by combining Eqs. (61)–(63):

$$\phi = 4 \arctan(S/L). \quad (64)$$

The geometrical parameters L and S can be measured in our simulation results. S is measured as the distance from $h_\alpha = 0.5$ on the top edge of the α particle to $h_\alpha = 0.5$ on the bottom edge of the particle, along the vertical line $x = 0$ through the center of the system. (Because the circular initial condition was exactly centered in the simulation domain, the thickest portion of the particle in the y direction is expected to remain along this vertical line; this was verified by measuring the thickness along the edges of adjacent elements located at $x = -0.5$ and $x = 0.5$.) The location along $x = 0$ where $h_{\alpha 1} = 0.5$ was determined through linear interpolation of the shape functions representing $\eta_{\alpha 1}$, $\eta_{\beta 1}$, and $\eta_{\beta 2}$ and calculation of the resulting h_α . Similarly, L is measured along the horizontal line $x = 0$ through the center of the system. However, because in the present model the order parameters are not constrained to sum to 1 at each position, the definition of where the left and right edges of the particle are located is not completely clear. This leads to uncertainty in measurement of L due to the diffuse interface description that is large relative to the uncertainty in the measurement of S . We choose the points $h_\alpha = 1/3$, $h_\beta = 2/3$ as the edges of the particle (which corresponds to $\eta_{\alpha 1} = \eta_{\beta 1} = \eta_{\beta 2} = 0.270$ for the simulation shown in Fig. 1). To estimate the effect of the uncertainty ΔL on the measurement of ϕ^{sim} , we assume that the location of the left and right edges of the particle cannot be determined any more accurately than half the characteristic thickness of the grain boundary, $\ell_{\beta 1\beta 2}/2$. The uncertainty in the measurement

TABLE II. Parameters for α - β system used for model verification. Measured dihedral angles ϕ^{sim} are within estimated measurement uncertainty $\Delta\phi^{\text{sim}}$ of the analytical prediction ϕ^{an} .

| κ | m | $\gamma_{\alpha\beta}$ | $\ell_{\beta1\beta2}$ | ϕ^{an} | ϕ^{sim} | $\Delta\phi^{\text{sim}}$ |
|----------|-----|------------------------|-----------------------|--------------------|---------------------|---------------------------|
| 1.0 | 1.0 | 4.5 | 2.82 | 135° | 131.6° | 6.3° |
| 0.5 | 1.0 | 4.5 | 2.0 | 135° | 133.3° | 4.2° |
| 0.5 | 0.5 | 4.5 | 2.82 | 135° | 132.1° | 5.7° |
| 0.5 | 1.0 | 1.5 | 2.0 | 120° | 118.3° | 3.4° |
| 0.5 | 1.0 | 0.9988 | 2.0 | 105° | 103.3° | 2.7° |

of the angle, $\Delta\phi^{\text{sim}}$, is given by

$$\Delta\phi^{\text{sim}} = \sqrt{\left(\frac{\partial\phi^{\text{sim}}}{\partial L}\right)^2 (\Delta L)^2} = \frac{4}{1 + \left(\frac{S}{L}\right)^2} \frac{S}{L^2} \Delta L, \quad (65)$$

where $\Delta L = \ell_{\beta1\beta2}/2$ is the uncertainty in the measurement of L , and the uncertainty in S has been neglected. Since the interface width is a function of κ and m , we perform a series of simulations to test the effects of κ and m on ϕ^{sim} . The results and associated uncertainties are summarized in Table II. All the listed values of ϕ^{sim} are in a reasonable range comparing with their analytical counterparts.

Another two simulations are performed with different values of $\gamma_{\alpha\beta}$, and results are also included in Table II. Similar to the previous cases, the dihedral angle measured in the simulation differs slightly than that from energetic calculations, which is due to the diffuse interface description in the phase-field model as discussed above. From above simulation results, the morphologies of the grain boundary allotriomorphs are well captured in our multiphase grand-potential-based model, with the predicted dihedral angles agreeing with classical geometrical and energetic analyses within estimated measurement uncertainty.

Another test case was conducted to demonstrate that the model is able to capture the different morphologies of corner (triple-junction) and edge (grain boundary) second-phase particles. In this simulation, a hexagonal matrix grain structure with four different α -phase grains (order parameters) and periodic boundary conditions in two dimensions was used. The system size was 512×512 , and initially circular β particles of radius 15 were distributed on both grain boundaries and triple junctions. It was assumed the interfacial and grain boundary energies are equal, as may be encountered for incoherent α - β interfaces and random high-angle grain boundaries between α grains [56]. The same parameters summarized in Table I were used, along with $m = \kappa = 1.0$ and $\gamma_{\alpha\beta} = \gamma_{\alpha\alpha\beta} = 1.5$. Uniform finite elements with $\Delta x = \Delta y = 0.5$ were used, since converged particle morphologies were obtained for particles with the same parameters and initial radius 10 previously in this section. The α -phase matrix was supersaturated in the initial conditions, with an initial composition $c_A = 0.15$ compared with the bulk equilibrium composition $c_A^{\alpha,\text{eq}} = c_A^{\alpha,\text{min}} = 0.1$, while the β phase precipitates had initial composition $c_A = 0.9$ equal to the bulk equilibrium composition for the β phase. After a short transient, the particles assume their expected shapes as shown in Fig. 2(a). While edge particles have the expected lenticular (consisting of two circular segments) shape, corner

particles have three circular segments with a triangular cross section [57]. The shape of corner particles also stems from the balance between interfacial and grain boundary energies that requires grain boundaries to enclose equal dihedral angles and form three tips [57].

Figures 2(b) and 2(c) show the continued evolution of the microstructure. Both corner and edge particles initially grow because of supersaturation. However, as supersaturation in the matrix decays, the coarsening stage is entered and corner particles start to grow at the expense of edge particles. This preferential coarsening results from the curvature difference that establishes a chemical potential gradient, driving matter from edge particles to corner particles. This could have a strong implication on grain growth kinetics in materials containing second-phase particles since it has been shown that corner particles are more effective in pinning grains than edge particles [58]. Hence, if coarsening of second-phase particles is active in such systems, grain growth will be hindered, which will make it difficult to achieve large grain sizes in such materials.

B. Stability of a two-phase interface

To verify that a two-phase interface is stable with respect to the formation of a third phase at the interface, a one-dimensional (1D) domain with the α , β , and δ phases is considered. The 1D domain ranges from $x = -15$ to $x = +15$ and is discretized with uniform elements with $\Delta x = 0.5$. A uniform time step $\Delta t = 1$ was used in this case. The initial conditions are an α - β interface with some amount of the δ phase present, as given by $\eta_{\alpha1} = \frac{1-\lambda}{2}[1 - \tanh(\frac{x}{\sqrt{2}})]$, $\eta_{\beta1} = \frac{1-\lambda}{2}[1 + \tanh(\frac{x}{\sqrt{2}})]$, and $\eta_{\delta1} = \lambda$, where $0 \leq \lambda \leq 0.1$. The initial condition for chemical potential was $\mu = 0$ throughout. We take $\kappa = m = 1$ and $\gamma_{\alpha1\beta1} = \gamma_{\alpha1\delta1} = \gamma_{\beta1\delta1} = 1.5$.

For the case $\lambda = 0$, the initial conditions are equivalent to the steady-state equilibrium interfacial profile given by Eqs. (35) and (36) with no δ phase present. It was verified that $\eta_{\delta1}$ remained at 0 as the system evolved in time, as expected from Sec. II C. The cases $\lambda = 0.005$, 0.05, and 0.1 were also simulated, corresponding to a small perturbation in $\eta_{\delta0}$ in the initial conditions. In each case, $\eta_{\delta0}$ rapidly decreased to 0 throughout. An example of the evolution of the order parameters for the case $\lambda = 0.1$ is shown in Fig. 3. Thus, for the materials parameters considered here, the α - β interface is stable with respect to formation of the δ phase.

C. Kinetics

To verify the kinetic behavior of the model, the growth of a precipitate phase from a supersaturated matrix is simulated. Two geometries are considered for the kinetic verification: the growth of a plate of β phase from supersaturated α (1D configuration) and the growth of a spherical particle of β from supersaturated α [three-dimensional (3D) configuration]. In the 1D configuration, one-half of a growing plate of the β phase is simulated in a 1D domain ranging from $x = 0$ to $x = 5000$. The initial half-thickness T of the plate is 100. In the initial conditions, $\eta_{\beta1} = \frac{1}{2}[1 - \tanh(\frac{x-x_0}{\sqrt{2}})]$ and $\eta_{\alpha1} = \frac{1}{2}[1 + \tanh(\frac{x-x_0}{\sqrt{2}})]$, where $x_0 = 100$. The initial chemical potential is given by $\mu_A = \frac{1}{4}[1 + \tanh(\frac{x-x_0}{\sqrt{2}})]$, corresponding

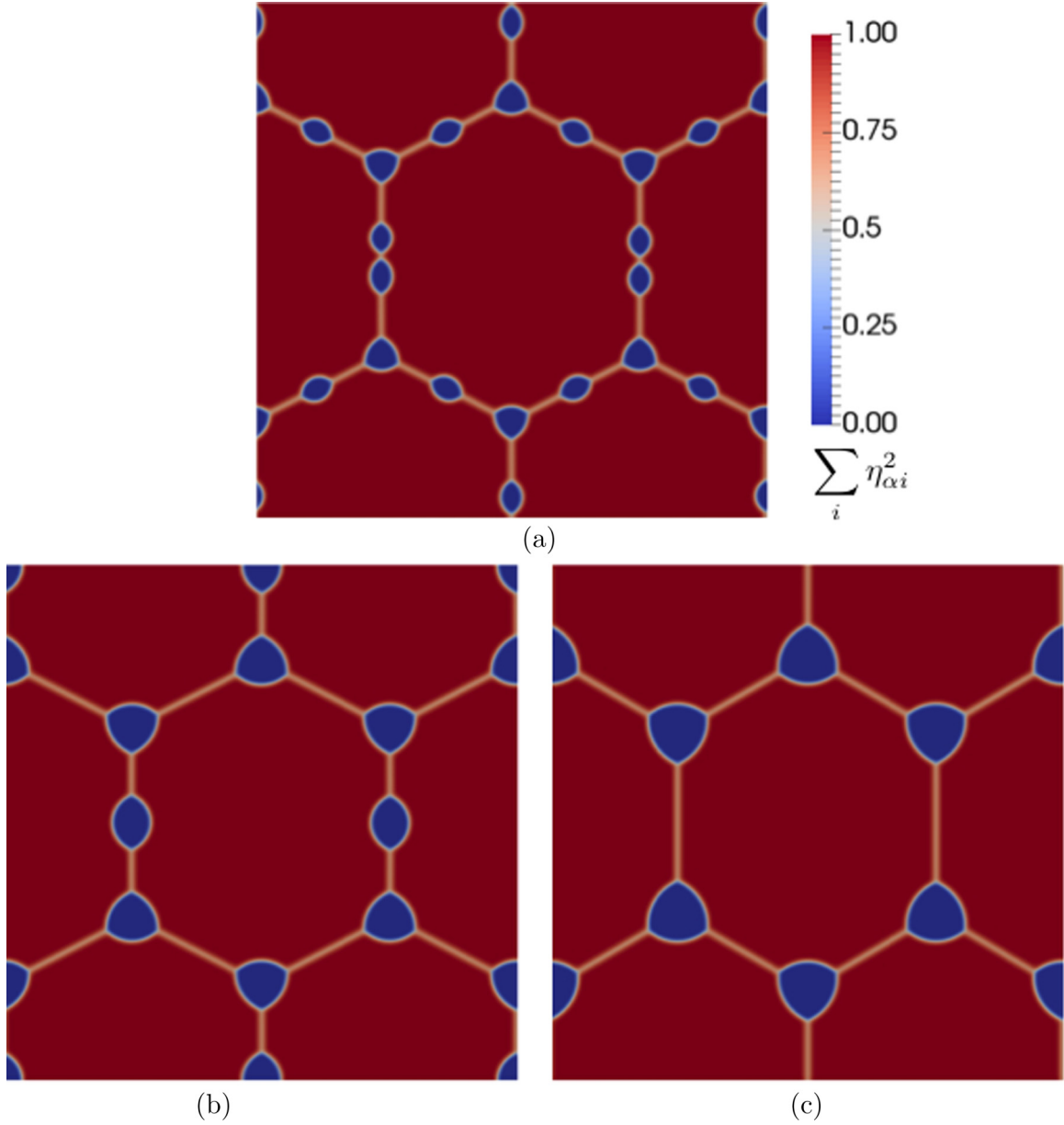


FIG. 2. Snapshots of growth and coarsening of β -phase particles from a supersaturated ($c = 0.15$) polycrystalline matrix. Simulation times are (a) $t = 50$, (b) $t = 100$, (c) $t = 150$. Corner (triple-junction) particles grow at the expense of edge (grain boundary) particles because of the effect of curvature. The color bar represents the value of $\sum_i \eta_{\alpha i}^2$, and is used to provide a visualization of the microstructure. The color bar is applicable to each subfigure.

to $c_A = 0.9$ in the precipitate and $c_A = 0.15$ in the matrix. This supersaturation causes the precipitate to grow in the $+x$ direction. No-flux boundary conditions are used on both ends of the domain.

The results of the 1D simulations are shown in Fig. 4(a). An analytical solution is available for this configuration [59], which predicts $T = \alpha_1 \sqrt{Dt}$, where t is the time and

$$\alpha_1 = K_1 \frac{(c_A^m - c_A^\alpha)}{(c_A^\beta - c_A^m)^{\frac{1}{2}} (c_A^\beta - c_A^\alpha)^{\frac{1}{2}}}, \quad (66)$$

where $c_A^\alpha = 0.1$ is the atomic fraction of A in the α phase at the $\alpha - \beta$ interface, $c_A^\beta = 0.9$ is the atomic fraction of A in the β phase at the $\alpha - \beta$ interface, and $c_A^m = 0.15$ is the

atomic fraction of A in the supersaturated matrix far from the interface. K_1 is a numerical constant with a value of 1.13 for the values of c_A^α , c_A^β , and c_A^m used.

As shown in Fig. 4(a), the expected linear relationship between T and \sqrt{t} is observed for $\Delta x = 1$ (the characteristic interface thickness used in these simulations was $\ell_{\alpha\beta 1} = 2.82$). The slope of a least-squares fit to this data was $0.073 \pm 8.0 \times 10^{-5}$, in good agreement with the prediction of the analytical solution of $\alpha_1 \sqrt{D} = 0.073$.

To quantify the effect of mesh resolution on the accuracy of the results, the simulations were repeated with coarser mesh spacings. As shown in the inset to Fig. 4(a), when $\Delta x = \ell_{\alpha\beta 1}/2 = 1.41$, T begins to deviate from linear behavior with respect to \sqrt{t} , showing periodic increases

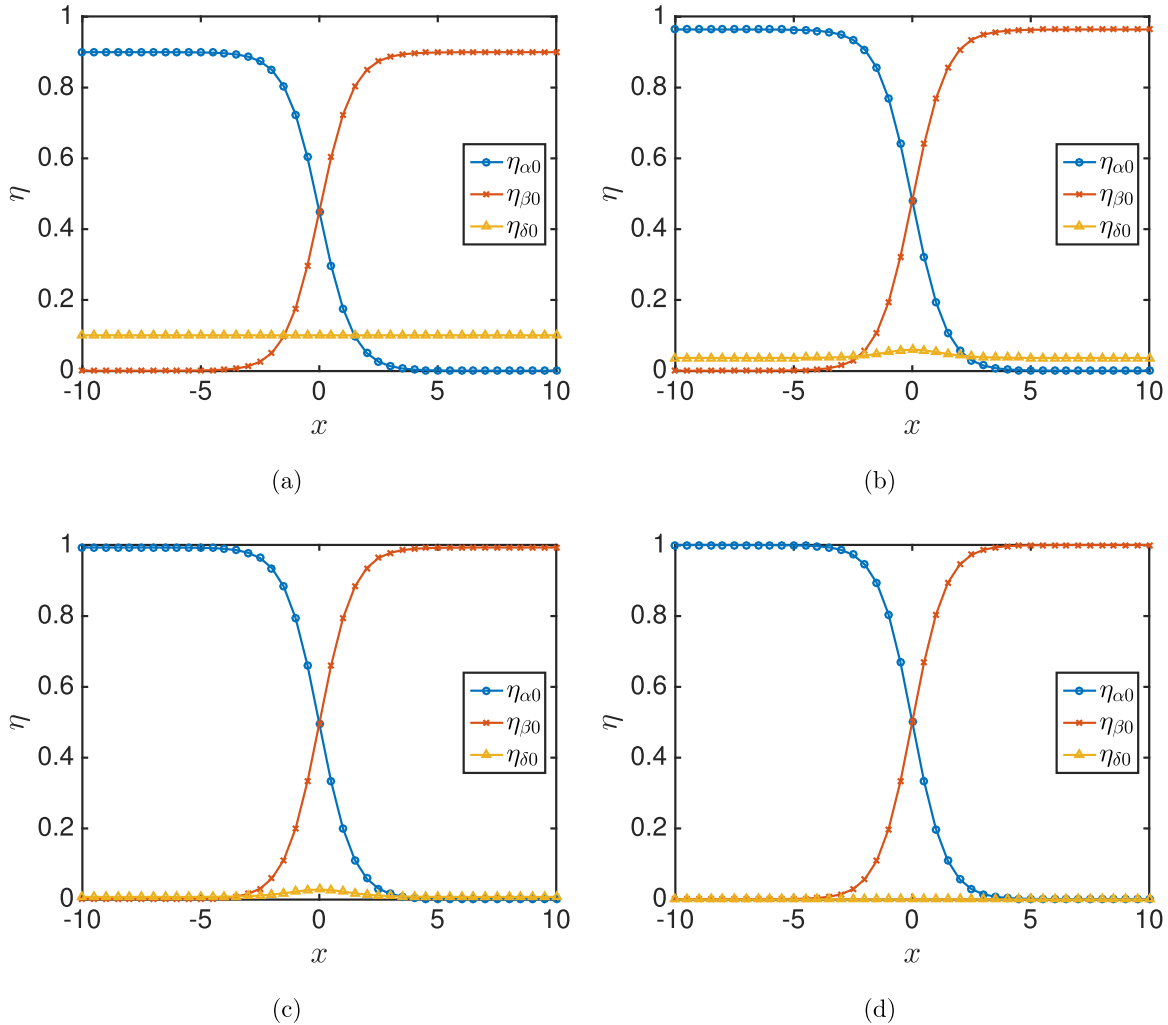


FIG. 3. Simulation of the evolution of a nonequilibrium α - β interface with $\eta_{\delta 1} = 0.1$ in the initial conditions. Simulation times are (a) $t = 0$, (b) $t = 1$, (c) $t = 2$, (d) $t = 5$. $\eta_{\delta 1}$ decreases to 0 and the α - β interface evolves to the equilibrium interfacial profile, demonstrating that for the materials parameters considered here, the α - β interface is stable with respect to formation of a third phase.

and decreases in the growth rate as the interface between phases becomes insufficiently resolved. When $\Delta x = 2$, the magnitude of oscillations in growth rate increases, and the deviation of T from the $\Delta x = 1$ simulation becomes significant.

In the 3D configuration, a spherical β particle of initial radius $r_0 = 100$ grows into the supersaturated α matrix. The simulation domain is spherical, ranging from $R = 0$ to $R = 5000$, and symmetric spherical coordinates are used. No-flux boundary conditions are used. The initial conditions used hyperbolic tangent functions as in the 1D configuration, and the matrix composition was again supersaturated to $c_A = 0.15$.

The results of the 3D simulations are shown in Fig. 4(b). For growth of a spherical precipitate, the analytical solution [59] predicts particle radius $r = \alpha_3 \sqrt{Dt}$, where

$$\alpha_3 = K_3 \frac{(c_A^m - c_A^\alpha)^{\frac{1}{2}}}{(c_A^\beta - c_A^m)^{\frac{1}{2}}}. \tag{67}$$

The initial particle radius of 100 is large enough that the Gibbs-Thomson effect on equilibrium compositions can be neglected, and again $c_A^\alpha = 0.1$, $c_A^m = 0.15$, and $c_A^\beta = 0.9$. For these values, $K_3 = 1.59$.

As shown in Fig. 4(b), after an initial transient, the expected linear relationship between r and \sqrt{t} is observed. Consistent with the results of Ref. [13], the initial transient for 3D simulations was much longer than for the 1D simulations. A least-squares fit to the data for $\sqrt{t} > 400$, $\Delta x = 1$ had slope $0.413 \pm 2.7 \times 10^{-5}$, in good agreement with the prediction of $\alpha_3 \sqrt{D} = 0.410$ from the analytical solution. When coarser meshes were used, oscillations in growth rate were observed as in the 1D case, although their magnitude was smaller. Based on the 1D and 3D results, a ratio of interface thickness to mesh spacing of approximately 3 or greater is recommended, although it should be noted that the interfaces considered in this section had either zero or relatively low curvature (for 1D and 3D cases, respectively). It should also be noted that identical results were obtained for $L_{\alpha\beta 1} = L_{\alpha\beta 1}^{\text{eq}} = 0.21$ and $L_{\alpha\beta 1} = 1$. In Ref. [13] instability in the order parameters

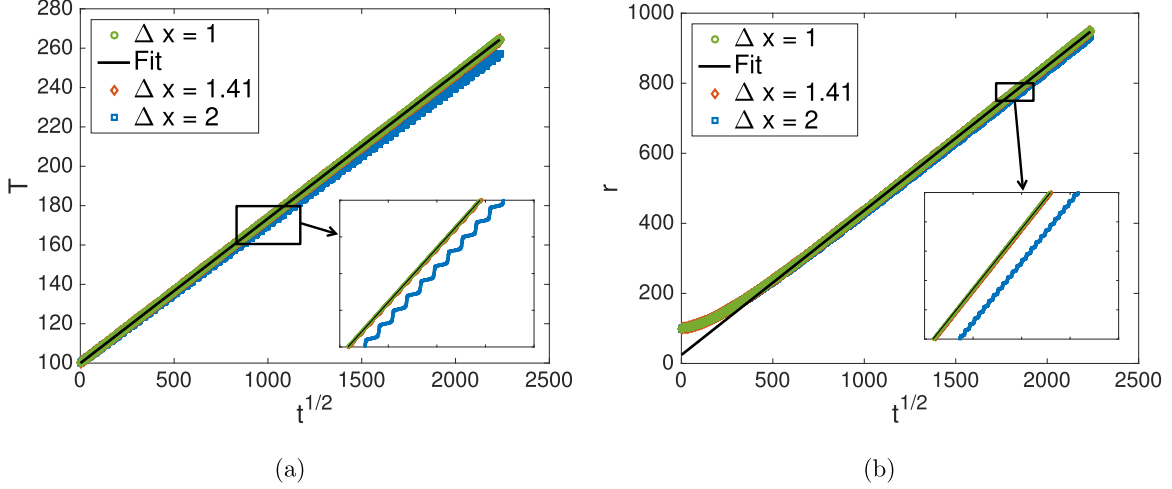


FIG. 4. Simulations of growth of β phase from supersaturated α phase (parameters given in Table I, with $c_A = 0.9$ in the β phase and $c_A = 0.15$ in the α phase). (a) Growth of a plate of β phase (1D geometry). (b) Growth of a spherical precipitate of β phase (3D geometry). The fit is to the linear portion of the $\Delta x = 1$ results, and in each case the slope of the fit line is in good agreement with the analytical prediction. The inset shows the effect of decreasing mesh resolution to the point where the interface is no longer adequately resolved.

and detachment of the order parameters from the composition profiles was observed for $L_{\alpha 1 \beta 1} > L_{\alpha 1 \beta 1}^{\text{eq}}$. These phenomena were not observed here. This may be due to the fact that equal diffusivities were used in each phase, in contrast to Ref. [13], where the diffusivities in different phases varied by several orders of magnitude.

IV. PHASE SEPARATION

In this section we consider the capability of grand-potential based phase-field models to model phase separation. The phase stability can be examined using linear stability analysis of the phase-field kinetic equations. For the case where concentration is used as the sole phase-field variable (Cahn-Hilliard model), it is well known that spinodal instability takes place when the second derivative of the free energy becomes negative. This analysis has been generalized by San Miguel *et al.* [60] to systems with different types of phase transitions and where both conserved and nonconserved order parameters are coupled. Instead of repeating the linear stability analysis here for the grand-potential formulation, we transform the grand-potential model back to the classical free energy formulation and use the results of San Miguel to deduce its stability. Note that such a transformation always exists, but it can be derived analytically only for the special cases of parabolic or dilute solution free energies where concentration can be directly expressed in terms of chemical potential and phase-field variable [32].

For simplicity, we first consider phase separation by spinodal decomposition in a two-phase binary system. In this case, a single phase-field variable (order parameter) η is sufficient to distinguish between the phases, i.e., η equals 0 in the matrix or parent phase (α) and 1 in the precipitate or second phase (β). Similar to the original work by Plapp [32], the total grand potential can be expressed as

$$\Omega = \int_V [\omega_{\text{int}}(\eta, \nabla \eta) + \omega_{\text{bulk}}(\mu, \eta)] dV. \quad (68)$$

In the above, the interfacial grand potential has the regular form,

$$\omega_{\text{int}}(\eta, \nabla \eta) = m \eta^2 (1 - \eta)^2 + \frac{\kappa}{2} |\nabla \eta|^2, \quad (69)$$

and the bulk grand potential takes on the form

$$\omega_{\text{bulk}} = h(\eta) \omega_{\beta}(\mu) + [1 - h(\eta)] \omega_{\alpha}(\mu), \quad (70)$$

where the interpolation function has to satisfy the following conditions:

$$h(\eta = 0) = 0, \quad (71)$$

$$h(\eta = 1) = 1, \quad (72)$$

$$\left. \frac{dh}{d\eta} \right|_{\eta=0} = \left. \frac{dh}{d\eta} \right|_{\eta=1} = 0. \quad (73)$$

A few interpolation functions have been proposed in literature. However, as we will demonstrate below, the exact form of this function determines whether or not phase separation can be simulated. We assume here that the free energies of the phases have parabolic dependence on concentration as in the cases presented above. In this simple case, the solute concentration is related to the chemical potential and phase-field variable by [32]

$$c = c^{\text{eq}}(\eta) + \mu [h(\eta)/k_{\beta} + (1 - h(\eta))/k_{\alpha}]. \quad (74)$$

The first term on the right-hand side is the equilibrium concentration profile given by $c^{\text{eq}}(\eta) = h(\eta)c^{\beta} + [1 - h(\eta)]c^{\alpha}$. Therefore, if one is to construct a free energy-based phase-field model consistent with the grand-potential formulation above, the chemical potential dependence on concentration and phase-field variable must satisfy Eq. (74), that is, it has to take on the form

$$\mu(c, \eta) = \frac{c - c^{\text{eq}}(\eta)}{h(\eta)/k_{\beta} + [1 - h(\eta)]/k_{\alpha}}. \quad (75)$$

The total free energy can then simply be deduced by integrating $\frac{\partial f_{\text{bulk}}}{\partial c} = \mu(c, \eta)$ with respect to c using Eq. (75) and noting that the constant of integration is simply given by Eq. (69). This results in

$$f_{\text{bulk}}(c, \eta) = \frac{[c - c^{\text{eq}}(\eta)]^2}{2 \{h(\eta)/k_\beta + [1 - h(\eta)]/k_\alpha\}}, \quad (76)$$

and the total free energy is

$$\begin{aligned} F &= \int_V f_{\text{tot}}(\eta, \nabla \eta, c) dV \\ &= \int_V [f_{\text{int}}(\eta, \nabla \eta) + f_{\text{bulk}}(c, \eta)] dV, \end{aligned} \quad (77)$$

where

$$f_{\text{int}}(\eta, \nabla \eta) = m \eta^2 (1 - \eta)^2 + \frac{\kappa}{2} |\nabla \eta|^2. \quad (78)$$

One must keep in mind that the resulting free energy-based model derived here will also have the advantage of decoupling interfacial energy from bulk energy. In other words, there is only one unique way of interpolating the free energies of the phases [Eq. (76)] that guarantees this feature.

Before we present the stability analysis of the model discussed above, we simplify things further by requiring, without loss of generality, that the free energy parabolas of the two phases to have the same curvature $k_\alpha = k_\beta = \epsilon$, and the solute concentration to be normalized such that $c = 1$ in the precipitate phase and $c = 0$ in the matrix phase. After such simplification, Eq. (76) becomes

$$f_{\text{bulk}}(c, \eta) = \frac{\epsilon}{2} [c - h(\eta)]^2. \quad (79)$$

According to the linear stability analysis of San Miguel [60], the chemical spinodal instability can be inferred from the Hessian matrix of the total free energy density. Particularly, spinodal decomposition will proceed if the value of the determinant of the Hessian matrix calculated for the initial state is negative:

$$\det H(f_{\text{tot}}) = \frac{\partial^2 f_{\text{tot}}}{\partial c^2} \frac{\partial^2 f_{\text{tot}}}{\partial \eta^2} - \left[\frac{\partial^2 f_{\text{tot}}}{\partial c \partial \eta} \right]^2 < 0. \quad (80)$$

Now if we consider the initial state to be a supersaturated matrix ($\eta = 0, 0 < c < 1$) and taking into account the specific total free energy density of Eq. (77) and the requirements of Eqs. (71)–(73) on the interpolation function, the stability limit can be expressed as

$$2m - \epsilon \left. \frac{d^2 h}{d\eta^2} \right|_{\eta=0} c = 0. \quad (81)$$

In other words, phase separation via spinodal decomposition takes place if the concentration is higher than the critical spinodal concentration:

$$c > c^s = \frac{2m}{\epsilon \left. \frac{d^2 h}{d\eta^2} \right|_{\eta=0}}. \quad (82)$$

According to Eq. (82), the interpolation function has then a profound effect on the phase separation stage. For instance, if one considers the two most common forms used in literature, the results are completely different. The first commonly used

form is

$$h(\eta) = 3\eta^2 - 2\eta^3 \quad (83)$$

for which the spinodal concentration is $c^s = \frac{m}{3\epsilon}$. On the other hand, for the form

$$h(\eta) = \eta^3 (6\eta^2 - 15\eta + 10) \quad (84)$$

the spinodal concentration is infinite since the second order derivative vanishes, which means that this specific form cannot be utilized to describe phase separation.

Based on our analysis presented above, we conduct simulations of phase separation using a grand-potential phase-field model. We implement the two-phase grand-potential model described by Eqs. (68)–(70) and use the interpolation function given by Eq. (83). The kinetic equations are the same as the ones that appear in the original work by Plapp [32] and are solved using MOOSE as summarized in Sec. III.

Two simulations for two different spinodal decompositions were carried out. Note that for the simplified model we use here, the chemical potential and concentration are related by $\mu(c, \eta) = \epsilon[c - h(\eta)]$ via Eq. (79). Hence, the critical chemical potential that corresponds to the spinodal concentration is simply given by

$$\mu^s(c^s, \eta = 0) = \epsilon c^s. \quad (85)$$

In the first simulation, we use $m = 1.5$, $\epsilon = 1.0$, and hence $\mu^s = c^s = 0.5$, while in the second simulation we use $m = 0.5$, $\epsilon = 1.0$, and hence $\mu^s = c^s = 0.167$. In both simulations, the initial configuration was a supersaturated matrix close to the spinodal instability, i.e., $\eta = 0$, and $\mu = \mu^s + \delta$, where δ is a random fluctuation given by a uniform random number between $-0.1\mu^s$ and $+0.1\mu^s$. This corresponds to fluctuations in the range $0.45 \leq c \leq 0.55$ for $c^s = 0.5$ and $0.1503 \leq c \leq 0.1837$ for $c^s = 0.167$. The magnitude of initial composition fluctuations in physical systems undergoing spinodal decomposition may vary widely depending on the materials system and processing conditions; however, unstable fluctuations will grow regardless of their initial amplitude in spinodal decomposition [61], so the choice of initial magnitude should not change whether spinodal decomposition occurs in the present simulations. Snapshots of the phase separation process in these systems are shown in Fig. 5. For the case of high spinodal concentration (upper row), the emerging second phase has the usual lamellar structure, while for the low spinodal concentration (lower row), the emerging phase has a circular shape. The dependence of the morphology of the precipitates on spinodal concentration has been reported in literature before [62].

While the analysis presented here is for the simple case of a two-phase system, it can be adapted for a multiphase system using the formulation presented earlier in the paper. To demonstrate this, without loss of generality, we also consider a binary two-phase system. However, now there are two order

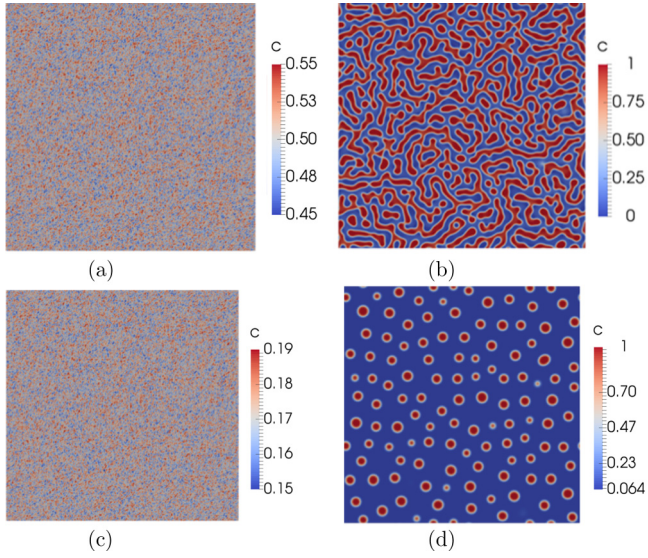


FIG. 5. Simulations of phase separation in a two-phase binary system using a grand-potential-based phase-field model with a single order parameter. Simulation times are (a),(c) $t = 0$; (b),(d) $t = 200$. The left column represents the initial configurations of the supersaturated matrix (see text), and the right column shows the concentration map after phase separation is complete. The upper row shows the morphology of second phase developed during separation for the case of high spinodal concentration ($c^s = 0.5$), and the lower row captures the morphology developed for the case of low spinodal concentration ($c^s = 0.167$).

parameters representing the two phases, η_β (the precipitate) and η_α (the matrix). Therefore the total grand potential is now given by

$$\Omega = \int_V [\omega_{\text{int}}(\eta_\beta, \eta_\alpha, \nabla\eta_\beta, \nabla\eta_\alpha) + \omega_{\text{bulk}}(\mu, \eta_\alpha, \eta_\beta)] dV. \quad (86)$$

The interfacial and bulk grand-potential densities now have the forms

$$\begin{aligned} \omega_{\text{int}}(\eta_\beta, \eta_\alpha, \nabla\eta_\beta, \nabla\eta_\alpha) &= m \left[\frac{1}{4} + \frac{\eta_\beta^4}{4} - \frac{\eta_\beta^2}{2} + \frac{\eta_\alpha^4}{4} - \frac{\eta_\alpha^2}{2} + \gamma_{\alpha\beta} \eta_\alpha^2 \eta_\beta^2 \right] \\ &+ \frac{\kappa}{2} [|\nabla\eta_\alpha|^2 + |\nabla\eta_\beta|^2], \end{aligned} \quad (87)$$

$$\omega_{\text{bulk}} = h_\beta(\eta_\beta, \eta_\alpha) \omega_\beta(\mu) + h_\alpha(\eta_\beta, \eta_\alpha) \omega_\alpha(\mu), \quad (88)$$

$$h_\alpha(\eta_\beta, \eta_\alpha) = \frac{\eta_\alpha^2}{\eta_\beta^2 + \eta_\alpha^2}, \quad (89)$$

$$h_\beta(\eta_\beta, \eta_\alpha) = \frac{\eta_\beta^2}{\eta_\beta^2 + \eta_\alpha^2}. \quad (90)$$

Now, following the same procedure described earlier in Sec. IV to derive the corresponding free energy consistent with this grand potential, one arrives at

$$\begin{aligned} F &= \int_V f_{\text{tot}}(c, \eta_\beta, \eta_\alpha, \nabla\eta_\beta, \nabla\eta_\alpha) dV \\ &= \int_V [f_{\text{int}}(\eta_\beta, \eta_\alpha, \nabla\eta_\beta, \nabla\eta_\alpha) + f_{\text{bulk}}(c, \eta_\alpha, \eta_\beta)] dV, \end{aligned} \quad (91)$$

$$\begin{aligned} f_{\text{int}}(\eta_\beta, \eta_\alpha, \nabla\eta_\beta, \nabla\eta_\alpha) &= m \left[\frac{1}{4} + \frac{\eta_\beta^4}{4} - \frac{\eta_\beta^2}{2} + \frac{\eta_\alpha^4}{4} - \frac{\eta_\alpha^2}{2} + \gamma_{\alpha\beta} \eta_\alpha^2 \eta_\beta^2 \right] \\ &+ \frac{\kappa}{2} [|\nabla\eta_\alpha|^2 + |\nabla\eta_\beta|^2], \end{aligned} \quad (92)$$

$$f_{\text{bulk}}(c, \eta_\beta, \eta_\alpha) = \frac{[c - c^{\text{eq}}(\eta_\beta, \eta_\alpha)]^2}{2[h_\beta(\eta_\beta, \eta_\alpha)/k_\beta + h_\alpha(\eta_\beta, \eta_\alpha)/k_\alpha]}, \quad (93)$$

$$c^{\text{eq}}(\eta_\beta, \eta_\alpha) = h_\beta(\eta_\beta, \eta_\alpha) c^\beta + h_\alpha(\eta_\beta, \eta_\alpha) c^\alpha. \quad (94)$$

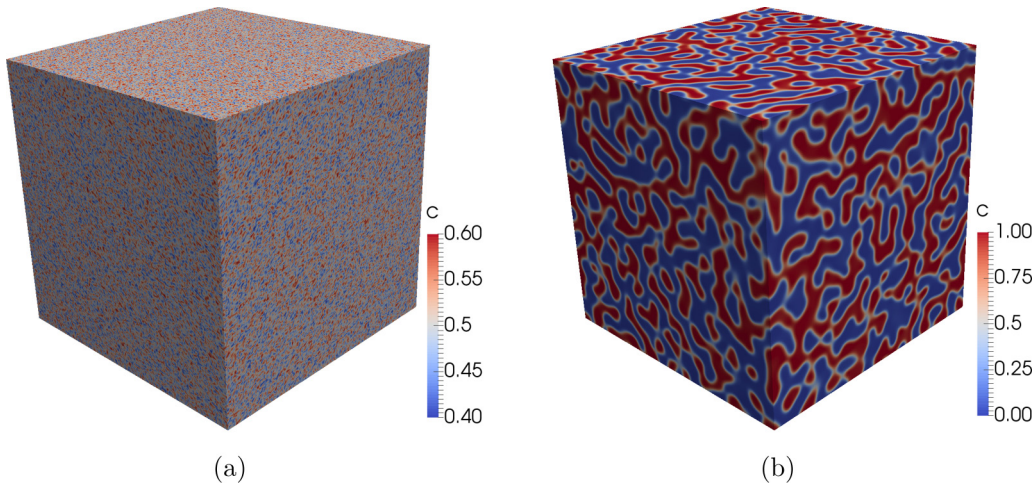


FIG. 6. Simulations of phase separation in a two-phase binary system using a grand-potential-based phase-field model with $\eta_\alpha = 1$, $\eta_\beta = 0$ representing the α phase, and $\eta_\alpha = 0$, $\eta_\beta = 1$ representing the β phase. (a) The initial condition of c ($t = 0$); (b) c after phase separation is complete ($t = 600$). The average concentration $c^{\text{avg}} = 0.5$ is above $c^s = 0.4$, so the system phase separates and forms a lamellar microstructure.

Moreover, the bulk free energy density can be simplified further if one follows the same assumptions that led to Eq. (79), i.e., the same curvature of parabola for the two phases and normalized concentration, and notes that $h_\alpha(\eta_\beta, \eta_\alpha) = 1 - h_\beta(\eta_\beta, \eta_\alpha)$. Specifically, Eq. (93) becomes

$$f_{\text{bulk}}(c, \eta_\beta, \eta_\alpha) = \frac{\varepsilon [c - h_\beta(\eta_\beta, \eta_\alpha)]^2}{2}. \quad (95)$$

The stability can then be determined from the Hessian matrix of the free energy as described previously in the current section, though the Hessian matrix here is a 3×3 matrix. The stability condition for an initially supersaturated matrix ($\eta_\beta = 0, \eta_\alpha = 1, 0 < c < 1$) is

$$c > c^s = \frac{m(2\gamma_{\alpha\beta} - 1)}{2\varepsilon}. \quad (96)$$

To demonstrate phase separation using the multiphase model, 3D simulations were performed of an α - β system with $\varepsilon = 1$ and normalized concentration, so that c^s is given by Eq. (96). Other parameters were $m = 0.4$ and $\gamma_{\alpha\beta} = 1.5$, resulting in $c^s = 0.4$, and $\kappa = 1$. The initial conditions for the order parameters were $\eta_\alpha = 1$ and $\eta_\beta = 0$, and the initial condition for μ was $0.5 + \delta$, where in this case δ is a uniform random number between -0.1 and 0.1 . This corresponds to fluctuations in the range $0.4 \leq c \leq 0.6$. The system size was $270 \times 270 \times 270$, with a uniform element size $\Delta x = \Delta y = \Delta z = 1.5$. The initial condition and microstructure after phase separation is shown in Fig. 6. Consistent with Fig. 5, the higher average composition $c^{\text{avg}} = 0.5$ results in a lamellar microstructure.

V. CONCLUSIONS

In this work, a multiphase, multi-order-parameter model has been developed based on a grand-potential functional. The advantages of this model are:

- (1) It removes the chemical energy contribution to interfacial energy, simplifying parametrization.
 - (2) It decouples interfacial energy and interfacial thickness, allowing the use of increased interface thickness and therefore improving computational efficiency.
 - (3) It prevents the spurious formation of additional phases at two-phase interfaces due to stability against third-phase perturbations.
 - (4) Additional phase concentration variables are not required as in the KKS approach, simplifying implementation.
- It is limited in the forms of chemical free energy that can be used, but this is not a severe limitation since parabolic functions can be used in this model, and more complex free energy functions are often approximated using such parabolic functions in phase-field modeling.
- The equilibrium behavior of the model was verified by comparing the simulated morphologies of second-phase particles at grain boundaries and triple junctions to the morphologies expected from the balance of interfacial and grain boundary energies. The kinetic behavior of the model was verified by comparing simulation results to the analytical solution for second-phase growth from a supersaturated matrix in 1D (plate morphology) and 3D (spherical morphology). Finally, we showed that phase-field models based on a grand-potential functional are capable of simulating phase separation and derived the conditions under which this is possible. Since this model is formulated for an arbitrary number of phases, grains, and chemical species, it is expected to be useful for simulating a broad range of materials systems.

ACKNOWLEDGMENTS

This work was funded by the Department of Energy Nuclear Energy Advanced Modeling and Simulation program. This manuscript has been authored by Battelle Energy Alliance, LLC under Contract No. DE-AC07-05ID14517 with the US Department of Energy. The United States Government retains and the publisher, by accepting the article for publication, acknowledges that the United States Government retains a nonexclusive, paid-up, irrevocable, world-wide license to publish or reproduce the published form of this manuscript, or allow others to do so, for United States Government purposes.

-
- [1] I. Steinbach, F. Pezzolla, B. Nestler, M. Seeßelberg, R. Prieler, G. J. Schmitz, and J. L. L. Rezende, *Physica D* **94**, 135 (1996).
 - [2] I. Steinbach and F. Pezzolla, *Physica D* **134**, 385 (1999).
 - [3] B. Nestler and A. A. Wheeler, *Phys. Rev. E* **57**, 2602 (1998).
 - [4] H. Garcke, B. Nestler, and B. Stoth, *SIAM J. Appl. Math.* **60**, 295 (1999).
 - [5] S. G. Kim, D. I. Kim, W. T. Kim, and Y. B. Park, *Phys. Rev. E* **74**, 061605 (2006).
 - [6] H. K. Kim, S. G. Kim, W. Dong, I. Steinbach, and B. J. Lee, *Modell. Simul. Mater. Sci. Eng.* **22**, 034004 (2014).
 - [7] G. I. Tóth, T. Pusztai, and L. Gránásy, *Phys. Rev. B* **92**, 184105 (2015).
 - [8] J. Hötzer, O. Tschukin, M. Ben Said, M. Berghoff, M. Jainta, G. Barthelemy, N. Smorchkov, D. Schneider, M. Selzer, and B. Nestler, *J. Mater. Sci.* **51**, 1788 (2016).
 - [9] B. Nestler and A. A. Wheeler, *Physica D* **138**, 114 (2000).
 - [10] B. Nestler, *J. Cryst. Growth* **275**, E273 (2005).
 - [11] B. Nestler, H. Garcke, and B. Stinner, *Phys. Rev. E* **71**, 041609 (2005).
 - [12] J. Eiken, B. Böttger, and I. Steinbach, *Phys. Rev. E* **73**, 066122 (2006).
 - [13] N. Moelans, *Acta Mater.* **59**, 1077 (2011).
 - [14] D. A. Cogswell and W. C. Carter, *Phys. Rev. E* **83**, 061602 (2011).
 - [15] P. C. Bollada, P. K. Jimack, and A. M. Mullis, *Physica D* **241**, 816 (2012).
 - [16] A. Choudhury and B. Nestler, *Phys. Rev. E* **85**, 021602 (2012).
 - [17] J. Kundin, R. Siquieri, and H. Emmerich, *Physica D* **243**, 116 (2013).
 - [18] J. Hötzer, M. Jainta, P. Steinmetz, B. Nestler, A. Dennstedt, A. Genau, M. Bauer, H. Köstler, and U. Rude, *Acta Mater.* **93**, 194 (2015).
 - [19] P. Steinmetz, M. Kellner, J. Hotzer, A. Dennstedt, and B. Nestler, *Comput. Mater. Sci.* **121**, 6 (2016).

- [20] M. Kellner, I. Sprenger, P. Steinmetz, J. Hotzer, B. Nestler, and M. Heilmaier, *Comput. Mater. Sci.* **128**, 379 (2017).
- [21] Y. C. Yabansu, P. Steinmetz, J. Hotzer, S. R. Kalidindi, and B. Nestler, *Acta Mater.* **124**, 182 (2017).
- [22] K. D. Noubary, M. Kellner, P. Steinmetz, J. Hotzer, and B. Nestler, *Comput. Mater. Sci.* **138**, 403 (2017).
- [23] P. Steinmetz, M. Kellner, J. Hotzer, and B. Nestler, *Metall. Mater. Trans. B* **49**, 213 (2018).
- [24] P. Steinmetz, J. Hotzer, M. Kellner, A. Genau, and B. Nestler, *Comput. Mater. Sci.* **148**, 131 (2018).
- [25] M. J. Welland, E. Tenuta, and A. A. Prudil, *Phys. Rev. E* **95**, 063312 (2017).
- [26] A. A. Wheeler, W. J. Boettinger, and G. B. McFadden, *Phys. Rev. A* **45**, 7424 (1992).
- [27] J. Tiaden, B. Nestler, H. J. Diepers, and I. Steinbach, *Physica D* **115**, 73 (1998).
- [28] S. G. Kim, W. T. Kim, and T. Suzuki, *Phys. Rev. E* **60**, 7186 (1999).
- [29] S. G. Kim, W. T. Kim, T. Suzuki, and M. Ode, *J. Cryst. Growth* **261**, 135 (2004).
- [30] R. Folch and M. Plapp, *Phys. Rev. E* **72**, 011602 (2005).
- [31] M. Ohno and K. Matsuura, *Acta Mater.* **58**, 5749 (2010).
- [32] M. Plapp, *Phys. Rev. E* **84**, 031601 (2011).
- [33] I. Steinbach, *Modell. Simul. Mater. Sci. Eng.* **17**, 073001 (2009).
- [34] E. Miyoshi and T. Takaki, *Comput. Mater. Sci.* **112**, 44 (2016).
- [35] N. Moelans, B. Blanpain, and P. Wollants, *Phys. Rev. B* **78**, 024113 (2008).
- [36] J. O. Andersson and J. Ågren, *J. Appl. Phys.* **72**, 1350 (1992).
- [37] C. H. P. Lupis, *Chemical Thermodynamics of Materials* (North-Holland, New York, 1983).
- [38] N. Moelans Web page, <http://nele.studentenweb.org/docs/parameters.m>.
- [39] M. Hillert, *Phase Equilibria, Phase Diagrams, and Phase Transformations: Their Thermodynamics Basis* (Cambridge University Press, Cambridge, 1998).
- [40] S. G. Kim, *Acta Mater.* **55**, 4391 (2007).
- [41] D. Gaston, C. Newman, G. Hansen, and D. Lebrun-Grandie, *Nucl. Eng. Des.* **239**, 1768 (2009).
- [42] J. D. Hales, K. A. Gamble, B. W. Spencer, S. R. Novascone, G. Pastore, W. Liu, D. S. Stafford, R. L. Williamson, D. M. Perez, R. J. Gardner, A. Casagrande, J. Galloway, C. Matthews, C. Unal, and N. Carlson, BISON Users Manual, Tech. Rep. INL/MIS-13-30307, Rev. 3 (Idaho National Laboratory, 2016).
- [43] MOOSE Framework Github repository, <https://github.com/idaholab/moose>.
- [44] MOOSE framework grand potential model test, https://github.com/idaholab/moose/blob/devel/modules/phase_field/test/tests/GrandPotentialPFM/GrandPotentialMultiphase.i.
- [45] MOOSE Framework Web page, <http://mooseframework.org>.
- [46] E. B. Hawbolt and L. C. Brown, *Trans. Metall. Soc. AIME* **239**, 1916 (1967).
- [47] A. Pasparakis, D. E. Coates, and L. C. Brown, *Acta Metall.* **21**, 991 (1973).
- [48] C. Atkinson, H. B. Aaron, K. R. Kinsman, and H. I. Aaronson, *Metall. Trans.* **4**, 783 (1973).
- [49] J. R. Bradley and H. I. Aaronson, *Metall. Mater. Trans. A* **8**, 317 (1977).
- [50] J. R. Bradley, J. M. Rigsbee, and H. I. Aaronson, *Metall. Mater. Trans. A* **8**, 323 (1977).
- [51] M. O. Tucker, *J. Nucl. Mater.* **78**, 17 (1978).
- [52] C. T. Walker, P. Knappik, and M. Mogensen, *J. Nucl. Mater.* **160**, 10 (1988).
- [53] I. Zacharie, S. Lansart, P. Combette, M. Trotabas, M. Coster, and M. Groos, *J. Nucl. Mater.* **255**, 92 (1998).
- [54] R. J. White, *J. Nucl. Mater.* **325**, 61 (2004).
- [55] P. C. Millett, M. R. Tonks, S. B. Biner, L. Z. Zhang, K. Chockalingam, and Y. F. Zhang, *J. Nucl. Mater.* **425**, 130 (2012).
- [56] D. A. Porter and K. E. Easterling, *Phase Transformations in Metals and Alloys* (Nelson Thornes, Cheltenham, United Kingdom, 1992).
- [57] E. Petrishcheva and J. Renner, *Acta Mater.* **53**, 2793 (2005).
- [58] K. Ahmed, M. Tonks, Y. F. Zhang, B. Biner, and A. El-Azab, *Comput. Mater. Sci.* **134**, 25 (2017).
- [59] C. Zener, *J. Appl. Phys.* **20**, 950 (1949).
- [60] M. San Miguel, J. D. Gunton, G. Dee, and P. S. Sahni, *Phys. Rev. B* **23**, 2334 (1981).
- [61] J. W. Cahn, *Acta Metall.* **9**, 795 (1961).
- [62] A. M. Somoza and C. Sagui, *Phys. Rev. E* **53**, 5101 (1996).